

A modular massively parallel computing environment for three-dimensional multiresolution simulations of compressible flows

Nils Hoppe^{1,*}, Stefan Adami¹, Nikolaus A. Adams¹

*Chair of Aerodynamics and Fluid Mechanics, Boltzmannstr. 15, D-85748 Garching bei
München*

Abstract

Numerical investigation of compressible flows faces two main challenges. In order to accurately describe the flow characteristics, high-resolution non-linear numerical schemes are needed to capture discontinuities and resolve wide convective, acoustic and interfacial scale ranges. The simulation of realistic three-dimensional (3D) problems with state-of-the-art finite-volume methods (FVM) based on approximate Riemann solvers with weighted non-linear reconstruction schemes requires the usage of high-performance computing (HPC) architectures. Efficient compression algorithms reduce computational and memory load. Fully adaptive multiresolution (MR) algorithms with local time stepping (LTS) have proven their potential for such applications. While modern central processing units (CPUs) require multiple levels of parallelism to achieve peak performance, the fine grained MR mesh adaptivity results in challenging compute/communication patterns. Moreover, LTS incur for strong data dependencies which challenge a parallelization

*Corresponding author

Email address: `nils.hoppe@tum.de` (Nils Hoppe)

strategy.

We address these challenges with a block-based MR algorithm, where arbitrary cuts in the underlying octree are possible. This allows for a parallelization on distributed-memory machines via the Message Passing Interface (MPI). We obtain neighbor relations by a simple bit-logic in a modified Morton Order. The block-based concept allows for a modular setup of the source code framework in which the building blocks of the algorithm, such as the choice of the Riemann solver or the reconstruction stencil, are interchangeable without loss of parallel performance. We present the capabilities of the modular framework with a range of test cases and scaling analysis with effective resolutions beyond one billion cells using $\mathcal{O}(10^3)$ cores.

Keywords: multiresolution, compressible flows, high-order methods, HPC, distributed-memory parallelization

1. Introduction

Physically accurate numerical investigation of compressible flows requires powerful flow solvers, both in terms of discretization techniques as well as computational efficiency. Key requirements for such a solver are vanishing artificial smearing of flow states, non-oscillatory treatment of discontinuities (e.g. shocks), and enforcement of discrete conservation. FVM combined with high resolution weighted essentially non-oscillatory (WENO) type reconstruction stencils [1] have proven their suitability to study compressible flows [2, 3, 4, 5] and are considered in this work. However, the numerical load of such solvers applied to practical compressible flow problems is high. Hence, the usage of compression algorithms and HPC compute sys-

tems is inevitable. Aiming for a generalized simulations platform covering a broad range of state-of-the-art schemes, we have developed a modular massively parallel computing strategy. Our framework enables efficient simulation of compressible flow applications and encompasses a wide range of high-resolution numerical schemes and fluid models for a user to choose from.

Even with the compute power of latest HPC clusters, fully resolved 3D simulations of compressible flows often are infeasible due to the high memory and computational requirements. Moreover, maximum resolution of the entire computational domain would be inefficient since resolution may be wasted in subdomains with little flow detail. Therefore, compression algorithms which locally adapt the mesh resolution have been developed. A well-known compression algorithm is the truncation-error based adaptive mesh refinement (AMR) [6] scheme. As its refinement is sensitive to the steepness of flow-field gradients, resolving regions of interest without strong gradient, e.g. contact or smooth rarefaction waves, requires special care. Wavelet-based methods achieve such a refinement automatically and often lead to a better mesh compression [7]. These algorithms are typically sorted into three groups: Wavelet-Galerkin, wavelet-collocation, and MR methods. As the first group does not inherently maintain conservation, we do not elaborate on it further and refer to the review paper of Schneider and Vasilyev [8]. Collocation schemes are based on second-generation wavelets and require a full wavelet-transformation [9]. They have been applied to hyperbolic [10] and parabolic [11] problems and have also been used to reach an adaptive compression in time [12]. Regarding their performance on HPC systems, collocation methods suffer from the wide support of active scales, which implies

non-local communications. Current developments try to address this issue by an asynchronous wavelet transform [13] at the cost of the vanishing moment property of the classic wavelet transform.

Interpolation-wavelet based MR was initially proposed by Harten [14] to reduce expensive flux computations in one dimension. This concept has been extended to viscous flows and to more dimensions [15, 16]. Harten’s algorithm has been further augmented to also save memory, e.g. , by the introduction of flux functions operating on non-equidistant points [17] or by introducing graded-tree concepts for hyperbolic [18] and parabolic equations [19]. For the latter approaches, various modifications have been presented, e.g., using a binary tree structure for n -dimensional meshes [20] or linking of reconstruction-stencil weights to the compression parameters [21]. Within the MR algorithm, further compression can be achieved via LTS schemes. Such methods were first introduced for single-stage methods [22] and then extended to explicit multi-stage Runge-Kutta (RK) schemes [23]. For the latter, also adaptive time step sizes have been introduced [24, 25]. In contrast to collocation methods, the support of active scales in interpolation-based wavelet MR is local. However, the number of communication partners per active scale is high and frequent neighbor-lookup can impede performance on HPC clusters, as explained later in more detail. Shared-memory implementations of this traditional single-scale approach have been presented for two-dimensional (2D) cases by Descombes et al. [26] and via MPI parallelization by Brix et al. [27].

Optimizing the communication patterns of a compression algorithm alone, however, does not suffice to harvest strong HPC performance [28]. For this,

all layers of parallelism in the modern compute hardware need to be addressed, from distributed to shared-memory as well as single instruction multiple data (SIMD) 'vectorization' parallelism [29]. Regarding vectorization, block-based schemes have proven their potential in the context of AMR methods [30] as well as for collocation methods [31]. For MR algorithms, blocking strategies have proven efficient for 2D cases using cell-centered FVM with a Threading Building Blocks (TBB) shared-memory parallelization [32] and for point-based finite difference schemes via MPI parallelization [33].

In this paper, we present a 3D block-based and fully-adaptive MR algorithm including adaptive local time stepping (ALTS) to solve hyperbolic and parabolic problems with FVM. The algorithm is parallelized using MPI. The implementation correctness, the achieved compression and the parallel performance of the algorithm are demonstrated on various test cases. Our algorithm is designed and implemented in a modular fashion, allowing to exchange the compute kernels easily without loss of parallel performance. We demonstrate this properly by combining different Riemann solvers (Roe [34], local Lax-Friedrichs (LLF) [35] and Harten-Lax-van Leer-contact (HLLC) [36]) with different reconstructions stencils (WENO [1], targeted essentially non-oscillatory (TEN0) [37], adaptive order weighted essentially non-oscillatory (WENO-AO) [38]) and several equations of state. We evaluate the parallel performance of the combinations on a large HPC compute cluster with more than a thousand cores and run simulations with more than a billion cells of effective resolution. Most MR implementations found in Literature [19, 24, 26, 33] are limited to cubic computational domains. Our implementation naturally allows to also simulate channel-like

domains.

We achieve the stated qualities via a combination of a modified Morton order [39] for efficient neighbor lookup combined with a level-wise space filling curve (SFC) for dynamic load balancing. In the data structure, we separate heavy computation data from the lightweight topology tree. In the octree we allow arbitrary tree cuts both horizontally and vertically. The algorithm is implemented in state-of-the-art C++17 code and is available under open-source license¹.

The remainder of this paper is structured as follows. First, the governing equations, their numerical discretization and the key concepts of MR and ALTS are revised in section 2. Next, in section 3, our modular block-based MR concept, the neighbor lookup and the load balancing scheme are presented. In section 4 we describe the detailed algorithm and highlight important implementation details. Section 5 states the conducted numerical verification with error analysis. Concluding remarks are given in the end.

2. Physical and numerical model

2.1. Governing Equations

A general conservation law in symbolic notation for a state vector \mathbf{U} is given by

$$\frac{\partial \mathbf{U}}{\partial t} + \nabla \mathbf{F}(\mathbf{U}) = S(\mathbf{U}), \quad (1)$$

¹<https://gitlab.lrz.de/nanoshock/ALPACA>

where $\mathbf{F}(\mathbf{U})$ and $S(\mathbf{U}, t)$ are the flux and source term vector, respectively. For the Euler equations, the state vector $\mathbf{U} = (\rho, \rho\mathbf{v}, E)$ contains the conserved quantities mass (concentration) ρ , momentum $\rho\mathbf{v}$ and total energy E . In these equations, \mathbf{v} is the velocity vector and the total energy is given by $E = \rho e + \frac{1}{2}\rho|\mathbf{v}|^2$, with the internal energy per unit mass e and the pressure p . To close the set of equations an additional equation of state (EOS) is needed. For demonstration purpose, in this work the stiffened gas equation [40]

$$p(\rho, e) = (\gamma - 1)\rho e - \gamma B \quad (2)$$

is used unless noted otherwise. A wide range of EOS is implemented. In eq. (2), γ and B represent the ratio of specific heats and the background pressure, respectively.

2.2. Numerical Scheme

We solve the governing equations using finite volumes on Cartesian meshes with cubic cells in 3D. For lower dimensional problems only a single cell depth is used in the excess dimensions. The fluxes across the cell faces are computed via an approximate Riemann solver. For demonstration, we restrict ourselves to Roe [34], HLLC [36] and Rusanov-flux [35] type solvers. In the latter, only the two cells sharing a face are considered for the eigenvalues. Within the Riemann solvers, different reconstruction stencils can be used to increase the order of the scheme. For the presented computations the stated Riemann solvers are used with fifth-order WENO [41, 1], fifth-order TENO [37] or fifth-order WENO-AO [38] discretization schemes.

2.3. Multiresolution Algorithm with Adaptive Local Time Stepping

On dyadically refined grids with infinite levels of refinement $l_m \in \mathbb{Z}$, a function $u(x, t)$ can be exactly represented by its MR representation in the form

$$u(x, t) = \sum_k c_k \theta_k(x, t) + \sum_m \sum_k d_k^{l_m} \psi_k^{l_m}(x, t), \quad (3)$$

where the subscript k samples the function at grid point $x_k^{l_m} = 2^{-l_m} k \in \mathbb{Z}$. The first sum over the products of scaling coefficients c_k and compact scaling functions θ_k defines the general shape of the function. The *details* d_k^l and the wavelet function ψ_k^l define the local fluctuations on the m -th refinement level l_m . By using interpolation wavelets, the details are given by mere difference of coarse and fine cell values

$$d_k^{l_m}(x) = \sum_k d_k^{l_m} \psi_k^{l_m}(x) = u_{l_{m+1}}(x) - u_{l_m}(x). \quad (4)$$

In his pioneering work, Harten [14] used this derivation to reduce the amount of costly flux computations with interpolated coarse grid states in regions with vanishing details

$$\|d^{l_m}\| < \varepsilon_{l_m}. \quad (5)$$

If the level-dependent threshold ε_{l_m} is chosen properly, the MR representation converges with a desirable order α . The convergence order of the applied numerical scheme thus is ensured by setting α equal to this convergence order considering both space and time. To do so, a reference level l_{ref} and reference threshold ε_{ref} need to be chosen. From these, ε_{l_m} is computed as

$$\varepsilon = 2^{-(\alpha+1)(l_{max}-l_{ref})}\varepsilon_{ref}, \quad (6)$$

$$\varepsilon_{l_m} = 2^{-D(l_{max}-l_m)}\varepsilon, \quad (7)$$

with the dimensionality D of the considered problem.

Fully adaptive MR schemes [18] remove cells with vanishing details from the grid to achieve high memory compression. These schemes naturally lead to octree data-structures. Following common notation, we call nodes in the tree *parent* if they are refined with *child* nodes on a higher level. Same-level neighboring nodes are called *brothers* if they share a parent, or *cousins* otherwise. A node is called a *leaf* if it does not have children. If a node does not have a cousin on one side we call this side a *resolution jump* or just *jump* for brevity. Leaf *refinement* is equivalent with creation of its finer grid structures in the tree. *Coarsening* means elimination of leafs which turns their parent into a leaf. Note, nodes are only coarsened together with all their brothers. We propagate information from level l_{m+1} down to level l_m using the conservative averaging operator

$$\mathcal{A}(u_{l_{m+1}}) \rightarrow u_{l_m} : u_{l_m} = \frac{1}{N} \sum_j^N u_{l_{m+1}}^j, \quad (8)$$

where N gives the number of children, e. g. four in 2D or eight in 3D.

Likewise, we define a prediction operation to propagate information form the lower level l_m to the higher level l_{m+1} . The prediction is defined locally and consistently, i. e. conservative with respect to the coarse grid cell averages. Mathematically, this is expressed as $\mathcal{A}(\mathcal{P}(u_{l_m})) = u_{l_m}$. We use the fifth-order accurate prediction

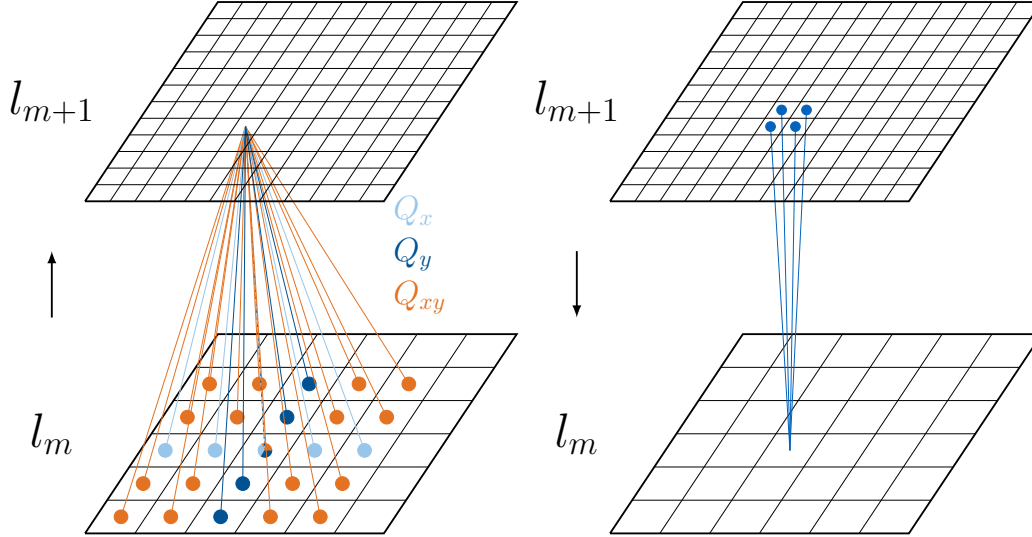


Figure 1: Prediction (left) and averaging (right) operators illustrated for a 2D grid. The finer mesh is plotted above the coarser one as it overlays this region in the computational grid.

$$\begin{aligned}
 \mathcal{P}(u_{l_m}) &\rightarrow u_{l_{m+1}}: \\
 u_{l_{m+1}}^{ijk} &= u_{l_m}^{ijk} + (-1)^i Q_x + (-1)^j Q_y + (-1)^k Q_z \\
 &\quad + (-1)^i (-1)^j Q_{xy} + (-1)^i (-1)^k Q_{xz} + (-1)^j (-1)^k Q_{yz} \\
 &\quad + (-1)^i (-1)^j (-1)^k Q_{xyz}.
 \end{aligned} \tag{9}$$

The respective Q -terms are given in the Appendix. Both operators are illustrated for a 2D mesh in fig. 1. The locality of the operators is clearly visible.

In addition to spatial compression, compute resources can also be saved by employing adaptive time stepping schemes. Therein, coarser cells are advanced with fewer, but larger time steps than fine ones. LTS schemes for MR [23] leverage the dyadic grid setup and obtain a level dependent time

step size

$$\Delta t_{l_m} = 2^{l_{max}-l_m} \Delta t_{l_{max}} \quad (10)$$

for the employed explicit multi-stage RK schemes. We call a time step on the finest level *micro time step* and a step on the coarsest level *macro time step*. In addition, ALTS schemes [24] adjust the time step sizes $\Delta t_{l_{max}}$ once all levels have advanced to the same point in time.

Here, we employ an improved ALTS scheme [25], where the local time-steps are adjusted after every micro time step. This is achieved by applying the averaging and prediction operation not only to conserved quantities, but also to the divergence of the numerical flux function directly.

3. Modular block-based MR algorithm

MR algorithms achieve high compression rates [18, 19, 23] when fine resolutions are required only in a fraction of the entire computational domain. In case of unsteady flows, however, the grid needs to be updated according to the given threshold ε_l at every micro time step. In a straightforward implementation, a single cell or scale may be coarsened or refined in each such time step. This, however, inhibits efficient execution of the algorithm on modern HPC CPU as it impedes two levels of parallelism: SIMD and distributed-memory. For both, the problem originates from (wide) stencil reconstruction. In a single-scale MR algorithm, i. e. where single cells are refined or coarsened, such stencils would cross resolution jumps, which implies either non-regular and possibly remote memory accesses, or introduction of *halo* cell buffers holding copies of the required values. Within a single-scale ap-

proach each cell potentially needs to be accompanied by a halo buffer, whose size is proportional to the stencil width. Allocating, filling and deallocating such single-scale halos, in particular by distributed-memory communication, is costly [27] and should be minimized.

For octree-based AMR and with wavelet collocation methods, block-based schemes have shown remarkable SIMD capabilities and overall application speedups [30, 42]. Hence, we introduce a similar blocking concept to our MR tree. Therein, each node in the octree holds one block with a fixed number of cells. Blocks at different levels differ only by their cell size, namely $\Delta x_{l_m} = 2^{-p} \Delta x_{l_{m+p}}$ (Δy and Δz respectively). To allow parallel computations on blocks we also add halo cells around each block. The amount of halo cells is dependent on the width of the used stencil. In this work, we use four halo cells at each block boundary which suffices for the employed 5th-order reconstruction schemes. In contrast to the single-scale halos, the ratio of compute-to-halo cells is thereby immensely improved and cell-neighbor lookups require only local array accesses. In a first analysis, we found our block-based approach capable to effectively utilize modern CPU SIMD capabilities [43]. In the physical domain, halo cells overlap the *internal cells (IC)* of the neighboring blocks. If two blocks with different cell sizes touch, the respective finer halo cells are filled with predicted values from the parent's block, otherwise the brother's or cousin's cell values are copied. Figure 2 illustrates these communication patterns together with the block-mapping at the coarsest level for a simple 2D mesh, when we illustrate a channel-like domain of three blocks at level l_0 . The middle node is refined and one of the children is refined further. Each block has eight IC per dimension. Between

the right most block and the blocks on l_{max} , a resolution jump of height two is present. Cells inside the thick lines are IC, the ones around are the halo cells. For the blocks on level l_1 the different communication patterns are indicated. The crosshatch shows how halo cells facing a jump are filled via prediction, whereas the other cells are filled with copies from the respective brother node. Halo cells not highlighted on l_1 are part of the external boundary condition and are filled accordingly.

In our block-based algorithm, nodes are refined or coarsened whenever the used error norm for this block - including halos - exceeds the given threshold, c.f. eq. (5) e.g. , the l_∞ norm is chosen, the refinement or coarsening of a block is triggered as soon as any cell in the block does not meet the respective threshold. This ensures that approaching or steepening discontinuities are detected and the grid is refined accordingly as in single-scale MR algorithms. In addition, this halo-concept allows for arbitrary resolution jumps, without violating the graded-tree requirement [18] of single-scale MR algorithms.

Besides the favorable SIMD capabilities, our block-based approach is beneficial also with respect to distributed-memory parallelization. Concordant to our implementation, we follow the MPI terminology with *ranks* being the parallel workers running an instance of the program. The frequency of topological changes is reduced by treating a block as smallest inter-rank parallel unit. This also leads to larger grain sizes of the overall load distribution, which in turn reduce sequential operations [31]. With fewer topology changes, fewer load-balance operations are required, reducing parallelization overhead. Nevertheless, a well-distributed load is key to parallel performance. For the domain partitioning, we aim at high locality and compactness. Ideally, all

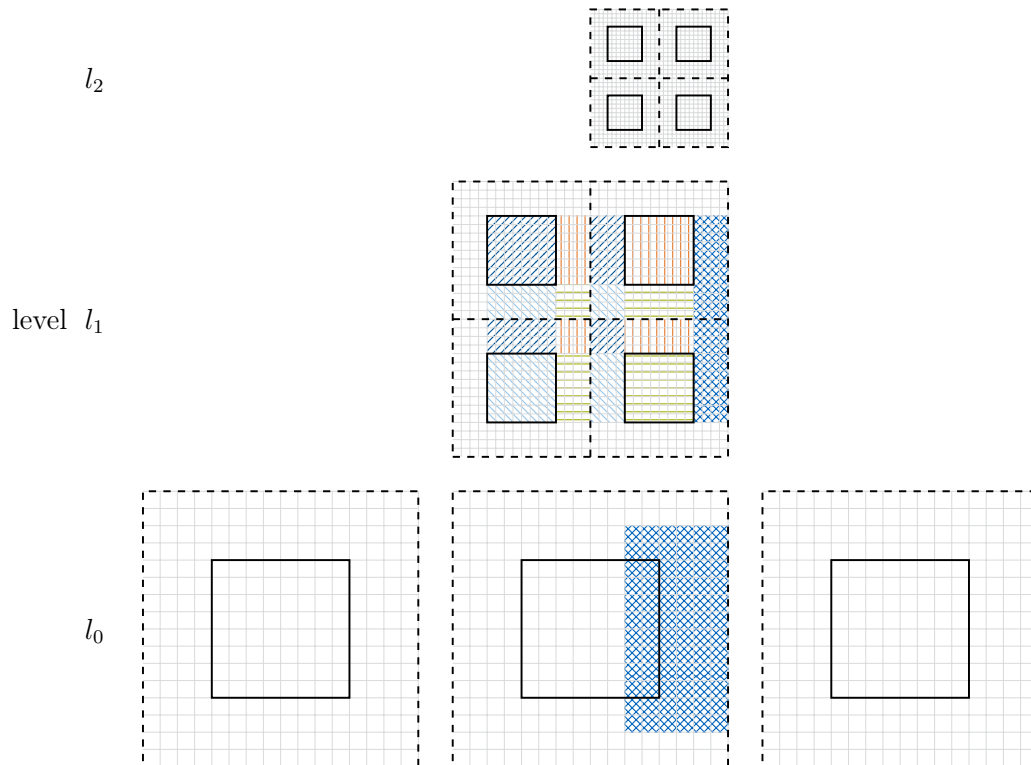


Figure 2: Internal data layout for a locally refined computational domain with $l_{max} = l_2$ with communication patterns for l_1 indicated.

nodes of one rank should be continuously grouped together and at the same time require communication with a limited set of other ranks only. When employing LTS these requirements are complemented by the demand, that the load needs to be well-balanced within each level of refinement. Otherwise, ranks could idle for several micro time steps if no blocks of the corresponding level are present.

We generate such partitions using a SFC [44], but do not simply bisect the curve into equal parts to distribute the nodes to ranks. Instead, a list of leaves-per-level is generated and ordered according to the SFC. These nodes in the list are then distributed to the available ranks. Thereby, an even load per level is obtained, while maintaining neighbor locality within a level. Exemplarily, fig. 3, illustrates the difference between the partitioning obtained using traditional Hilbert- [45] or Z-curves [39], and our level-wise modifications. In the figure, the domain matches a 2D quadtree refined once everywhere and two more times in the upper quadrant. The color scale and the small number in each node indicates on which rank the node resides. The SFC is illustrated which remains the same for the level-wise partitioning. In all cases, nodes are assigned to ranks by traversing the curve. On the right, also the level of the node is considered during the assignment to a rank. Clearly, the level-wise curve leads to a more scattered distribution, but in the traditional distribution whole ranks would idle for multiple micro time steps. For example, in the classical Z-curve distribution rank “two” holds only nodes at level l_1 and thus would idle for half of all micro time steps. The local regions within a level are also clearly visible in the figure. Once, the leaves are distributed as described, parents are recursively assigned to

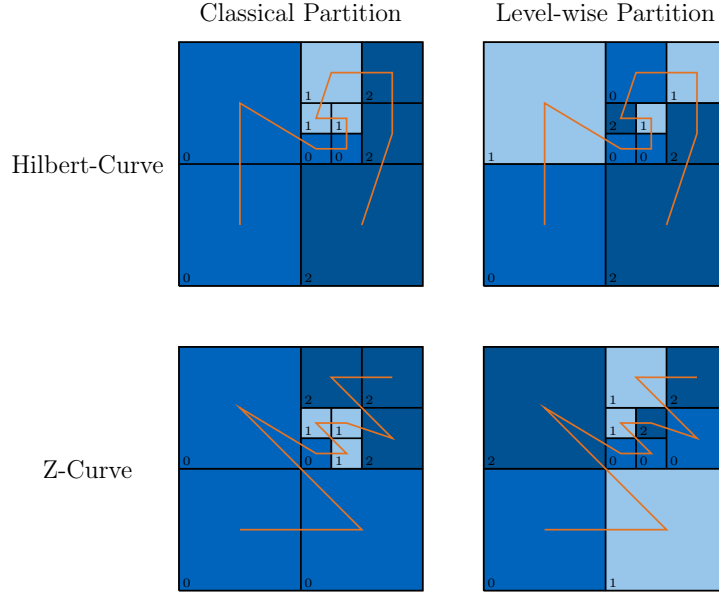


Figure 3: Domain partitioning via Hilbert- (top) or Z-curves (bottom) and their level-wise counterparts.

the rank where the majority of their children resides on.

Halo cells adjacent to partition borders are updated via communication. In order to identify communication partners and to store received data in the correct location, efficient neighbor lookups are necessary. For this purpose, a mapping which allows cheap identification of the neighboring nodes and fast rank-lookup is introduced. For octree structures, the Morton Order [39] offers the required functionality. Originally, each node is assigned a unique id in form of a bitstream like

$$\begin{array}{c}
 \text{z- and y-offset in } l_1\text{-group} \\
 0 \dots 0 \underbrace{001}_{l_2\text{-group}} \overbrace{110}^{l_1\text{-group}} \underbrace{010}_{l_0\text{-group}} .
 \end{array} \tag{11}$$

Note, this stream has the position on the respective level in the tree encoded.

In 3D, each three-bit long group indicates its positioning along the x , y and z -axis, respectively. As an example, the node at the origin of the coordinate axis on level l_0 is labeled 000, and the node with id 010 is positioned on top of the previous node in the y -axis without an offset in the other two directions. Parents of nodes are identified by simply shifting the id stream three bits to the right. Respectively, child ids are found by shifting the parent id three bits to the left and adding the bits of the new group to the shifted parent id. Furthermore, the respective bitstream 000 to 111 is added depending on the x -, y - and z -offset of the child within the new group. Neighbor lookups with similar simplicity are based on (concatenated) bitwise logic operations. We list the instructions to find the neighbor in positive direction along any axis as algorithm 1. In case the opposite neighbor on the same axis is to be found the last line changes to $f \leftarrow \overline{id_n[i]} \vee f$. This formulation can be seen as operating from right to left on every third bit of the stream thereby only changing the bits corresponding to one particular axis. If a one is encountered, the current and the next bits are flipped. Once a zero is flipped, the process terminates. An example is shown in Figure 4. Diagonal neighbor ids are determined by concatenating the instruction for the respective directions.

With the Morton order in-place, tree searches can be replaced by efficient hash-based lookups. This allows to split the 'light-weight' topology data and the 'heavy' computational data and map them by the Morton id. In case of inter-rank communication, the id-logic can be used to identify the communication partner and to tag asynchronous communication messages. Partitioning a mesh via Morton ordering, however, has its drawbacks. First, only cubic domains can be partitioned directly due to the embedded octree

Algorithm 1 Calculation of neighbor id_n form id

$N \leftarrow$ id bit length.

$d \leftarrow 0,1,$ or 2 for $x,y-$ or z -axis, respectively.

$id_n \leftarrow id$

$f \leftarrow 0$

for $i = d; i < N; i += 3$ **do**

$id_n[i] \leftarrow id_n[i] \bar{\vee} f$

$f \leftarrow id_n[i] \vee f$

end for

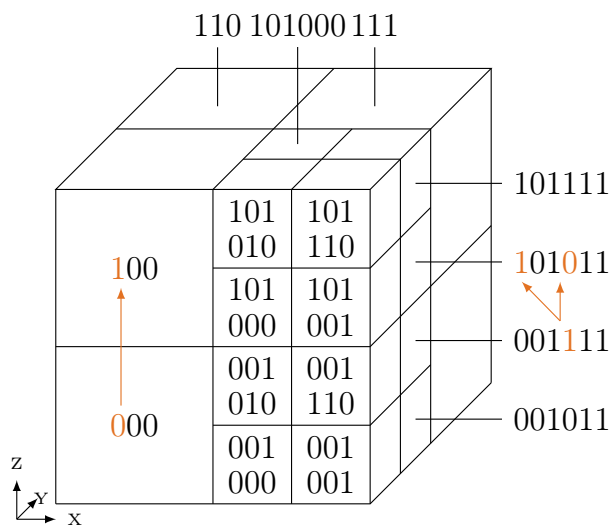


Figure 4: Morton Ordering for a cube. On the left and the right side the neighbor-lookup bit flipping is illustrated in orange.

structure. Second, the id 000 is not unique unless the size of the stream is measured in addition. We overcome both limitations by introducing the headbit 1, which is added from the left to the normal Morton index

$$0..01 \underbrace{101001010111}_{\substack{\text{headbit} \\ \text{as before}}}. \quad (12)$$

With the headbit in place, every zero-id is uniquely defined. The neighbor lookups still follow algorithm 1, yet the headbit is simply removed before the computation and then re-added to the final result. The level of an id is obtained by shifting the id one level-group to the right until only the headbit remains. Now the count of performed shifts minus one gives the level number. Additionally, introducing the headbit generalizes the Morton order for arbitrarily tiled geometries like, e. g. , channels or T-shapes. Such domains are embedded in a coarse zero-level octree with deactivated nodes. We call such deactivated nodes *shadow nodes*. Figure 5 shows a comparison of the two Morton ordering schemes for a 2D tree with three levels. As illustrated, using the headbit and two levels of shadow nodes allows to represent a channel with 6×2 nodes. The shadow levels do not need to be computed or stored; not even their light-weight topology data. Instead, a forest of trees starting on the first non-shadow level can be used. In this work, we use fixed-size 64-bit long ids with seven shadow levels. This allows us to simulate channels with length ratios up to $128 \times 1 \times 1$ and 13 levels of refinement.

4. Algorithm and Implementation

We have developed a modular, thus flexible, object-oriented programming (OOP) framework in C++11 to solve the previously described block-based

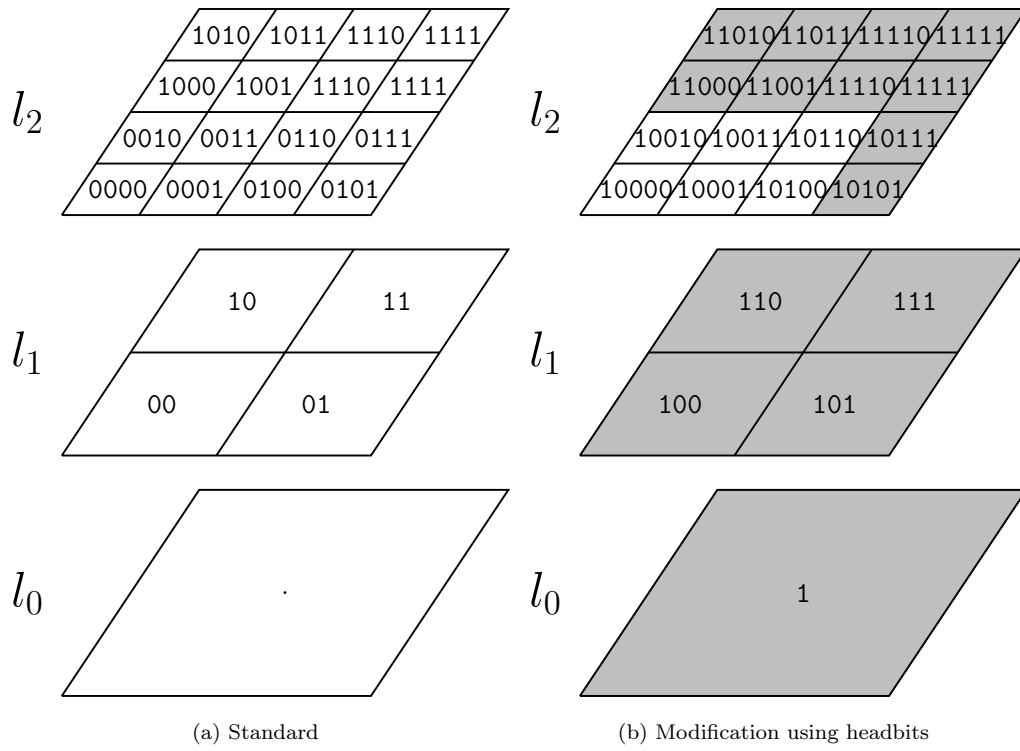


Figure 5: 2D tree indexed by standard morton order (a) and our proposed modification (b). Shadow nodes are indicated in gray. Note the double assignment of the id “zero” on the left.

MR algorithm. The core principle is separation of data containers and data manipulators. For simplicity, we restrict ourselves to blocks with the same amount of cubic cells per dimension, i.e. $\Delta x = \Delta y = \Delta z$. The `Block` class is the heavy data container, holding buffers for conservative and prime states. Note, storing prime states proved to outperform re-computations from conservative states for our implementation. In addition, six buffers for the fluxes across each surface of a block are reserved to ensure conservation at resolution jumps [19]. For the chosen fifth-order accurate prediction operator eq. (9) we use a multiple of four cells as IC in each block.

As proposed earlier, we split the topology and the compute heavy data. The topology is programmed as standard octree, which eases the execution of the SFC partitioning algorithm. Using the modified Morton order in a hash-map, the heavy data is connected to its respective topology data. The heavy data is local to one MPI rank. We employ template programming using the curiously recurring template pattern (CRTP) to change the Riemann solver or the reconstruction stencil at compile time. Similarly, the number of IC per block, the error norm eq. (5), the SFC and the activation of source terms in eq. (1) are specified at compile time. We applied design patterns like the proxy, the factory and the strategy pattern to change the initial and boundary conditions, the EOS, the fluid parameters and the MR threshold ε_{l_m} at runtime.

Ideally, the MR compression would be applied to the initial condition on a fully-refined grid. For the considered huge resolutions, however, this increases the needed compute memory manifold and contradicts employed fully-adaptive MR compression. Hence, we instead build the initial topology

bottom-up: the given initial condition is discretized level-by-level and MR compression is applied successively after each level. Our initialization routine is listed in algorithm 2. During node refinement, we allocate the memory of all children on the rank of the parent. Remember, the thresholding norm is evaluated for whole blocks. From algorithm 2 it is clear that no node on level l_1 is ever coarsened, i. e. a homogeneous mesh is created if the user sets $l_{max} = l_1$. This is necessary, as refinements to higher levels are based on the details computed between l_0 and l_1 , see eq. (4).

The compute loop is summarized in algorithm 3. We define the ordered sets of levels $\mathbb{L}_{all} = \{l_{max}, \dots, l_0\}$ and \mathbb{L} , with the first holding all levels and the latter holding the *active* levels (which change over time). The number of RK stages s , the integration weights b_i and the increments k_i depend on the order of the used RK scheme [25]. The maximum time step on the finest level is limited by the global Courant-Friedrichs-Lewy (CFL) criterion

$$\Delta t_{l_{max}} = k \cdot \frac{\Delta x}{\sum_i |||v_i| + c||_{\infty}}, \quad (13)$$

with the CFL number $k \leq 1$, the velocity in i -direction v_i and the cell-local speed-of-sound c . Note, eq. (13) can be extended to consider source terms if present in eq. (1). For a RK method of second-order, two sets of buffers for the conservatives variables are sufficient. For higher orders, however, a third permanent buffer needs to be included. The second averaging per RK-stage and the integration in halo cells, c. f. algorithm 4, is attributed to the ALTS scheme [25].

Algorithm 2 Initialization

$l_{max} \leftarrow$ user input

$\varepsilon_{l_m} \leftarrow$ from user inputs ε_{ref} and l_{ref} according to eqs. (6) and (7)

Initialize topology for level l_0 on all ranks

Allocate l_0 -blocks on respective rank

Impose initial condition on all l_0 -blocks

for $m = 1; l_m < l_{max}; ++ m$ **do**

 Refine all blocks of l_{m-1}

 Impose initial condition on all l_m -blocks

if $m > 1$ **then**

for All nodes on l_m **do**

if $\|d^l\| < \varepsilon_{l_m}$ **then**

 Coarsen respective node

end if

end for

end if

 Apply load balancing to re-distribute nodes

end for

Algorithm 3 Compute Loop

Final simulation time: $t_{end} \leftarrow$ user input

while $t < t_{end}$ **do**

$\mathbb{L} = \mathbb{L}_{all}$

for Micro time steps $r = 0; r < 2^{l_{max}}; ++r$ **do**

for all $l_m \in \mathbb{L}_{all}$ **do**

$\Delta t_{l_m} \leftarrow$ according to eqs. (10) and (13)

end for

for RK stages $s = 0; s < s_{max}; ++s$ **do**

for all leaves on $l_m \in \mathbb{L}$ **do**

$f(u_{l_m}) = \Delta x_{l_m} F(u_{l_m})$, according to eq. (1)

end for

for all nodes on $l_m \in \mathbb{L} \setminus \{0\}$ in descending order **do**

$\mathcal{A}(f(u_{l_m})) \rightarrow f(u_{l_{m-1}})$

end for

for all nodes on $l_m \in \mathbb{L}_{all}$ **do**

if resolution jump **then**

Fill halo cells by $\mathcal{P}(F(u_{l_{m-1}})) \rightarrow F(u_{l_m})$

else

Fill halo cells with copies of neighbor values

end if

end for

$\mathbb{L} = \{l_{max}, \dots, l_{max+1-\sum((r+1)\Downarrow r)}\}$

Integration according to algorithm 4

```

for all node on  $l_m \in \mathbb{L} \setminus \{\min(\mathbb{L})\}$  do
     $\mathcal{A}(F(u_{l_m})) \rightarrow F(u_{l_{m-1}})$ 
end for
if  $s = s_{max} - 1$  then
    for all leaves on  $l_m \in \mathbb{L}$  do
        if neighbor is on finer level then
            Adjust coarse cell values:
            
$$u_{l_{m-1}} = u_{l_{m-1}} - \Delta t_{l_m} F(u_{l_{m-1}}) + \Delta t_{l_m} \mathcal{A}(F(u_{l_m}))$$

        end if
    end for
end if
for all nodes on  $l_m \in \mathbb{L}$  do
    if !resolution jump then
        Fill halo cells with copies of neighbor values
    end if
end for
     $\mathcal{A}(u_{l_m}) \rightarrow u_{l_{m-1}} \forall m \in \mathbb{L} \setminus \{0\}$ 
end for
    refine and coarse mesh according to MR analysis eqs. (4), (5) and (7)
    re-distribute nodes according to load balancing strategy
     $t += \Delta t$ 
end for
    Write time step output (if desired)
end while

```

Algorithm 4 Integration according to Kaiser et al., 2019.

for all nodes on $l_m \in \mathbb{L}$ **do**

Integrate according to RK scheme: $u_{l_m} = u + \Delta t_{l_m} \sum_{i=0}^{i \leq s} b_i k_i$

if resolution jump **then**

Integrate in halo cells: $u_{l_m} = u + \Delta t_{l_m} \sum_{i=0}^{i \leq s} b_i k_i$

end if

end for

5. Benchmarking

We use an automated test suite to assess the physical correctness of our implementation. For demonstration, we show two such verifications in the following for a Sod shock tube and Rayleigh-Taylor instabilities (RTIs) problem section 5.1 before we evaluate the (parallel) numerical performance of our implementation. All these simulations were conducted on the CoolMUC2 Cluster at LRZ, consisting of 28-way Intel Xeon E5-2697 v3 codename “Haswell” based nodes with FDR14 Infiniband interconnect²³. We have varied the choice of the Riemann solver, the reconstruction stencil, the number of IC, the MR thresholding norm, and the EOS to demonstrate the flexibility of our framework. We introduce a “standard configuration” which uses the approximate Riemann solver of Roe with WENO-5 reconstruction stencil and 16^3 IC per block. The following runtime settings are chosen for this configuration: the l-infinity norm is used for MR thresholding with $l_{ref} = l_{max-1}$ and $\varepsilon_{ref} = 0.01$. The stiffened gas EOS with $\gamma = 1.4$ and $B = 0$ defines the

²<https://doku.lrz.de/display/PUBLIC/CoolMUC-2>

³<https://www.lrz.de/services/compute/linux-cluster/overview>

gas phase. Time is integrated with a CFL number of 0.6 using a second-order RK scheme. This standard configuration is used unless otherwise stated.

5.1. Sod shock tube

We assess the correctness of the implemented algorithm by studying the well-known one-dimensional Sod shock tube problem [46]. The Sod test case is characterized by evolution of three distinct waves along the x -axis. Therefore, an initial discontinuity with left $(\rho = 1.0, \mathbf{v} = 0, p = 1.0)_{x \leq 0.5}$ and right states $(\rho = 0.25, \mathbf{v} = 0, p = 0.125)_{x > 0.5}$, defines a Riemann problem in the computational domain of size $[0, 1.0] \times [0, 0.25] \times [0, 0.25]$. The final state at $t_{end} = 0.2$ is shown in Figure 6a. We simulate this problem using $l_{max} = l_i \forall i \in [0, 6]$ while keeping $l_{ref} = 4$ and $\varepsilon_{ref} = 0.01$ fixed. Thus, the resolution varies from 64 to 4096 (effective) cells in the coarsest and finest setup, respectively. We ensure that no spurious y - or z -momenta occur and compare our results against the known analytic solution. In Figure 6b, we plot the l_1 error-norm for density and velocity. The observed second-order convergence agrees with the employed order of the time-integration scheme. For a more detailed convergence study we refer to our previous work [25].

5.2. Rayleigh-Taylor instability

In the following section we analyze the RTI. The source-term implementation of the governing equation is validated with the analysis of the growth-rate prediction.

A heavy fluid with density ρ_h is placed on top of a lighter one with density ρ_l . If the interface between the fluids is disturbed, a mushroom-like instability can develop under the action of gravity. It is known [47, 48] that

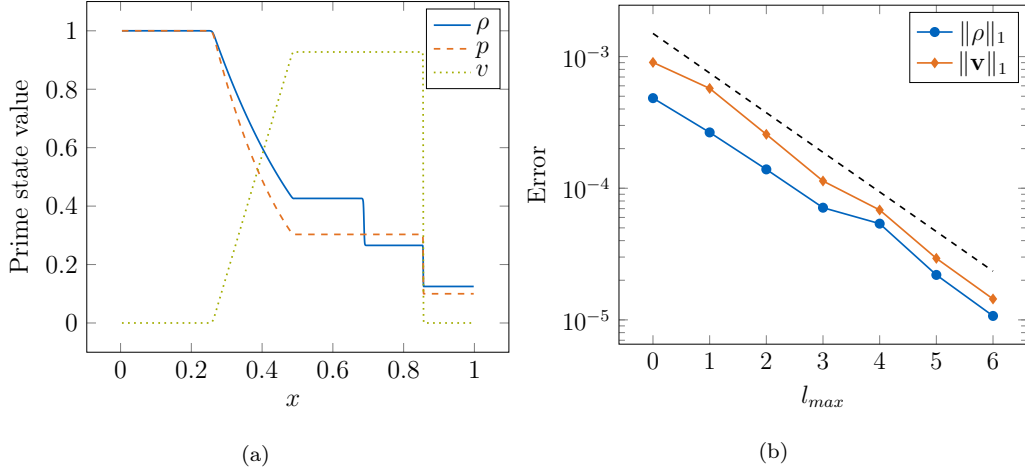


Figure 6: Prime state profiles of the Sod shock tube at $t=0.2$ (a) and corresponding error analysis (right).

the growth rate n depends on the wavenumber k of the disturbance. In the linear regime, n fulfills

$$\begin{aligned}
& - \left\{ \frac{gk}{n^2} \left[(\alpha_l - \alpha_h) + \frac{k^2 T}{g(\rho_l + \rho_h)} \right] + 1 \right\} (\alpha_h q_l + \alpha_l q_h - k) - 4k\alpha_l\alpha_h \\
& \quad + \frac{4k^2}{n} (\alpha_l \nu_l - \alpha_h \nu_h) \{ (\alpha_h q_l - \alpha_l q_h) + k(\alpha_l - \alpha_h) \} \\
& \quad + \frac{4k^3}{n^2} (\alpha_l \nu_l - \alpha_h \nu_h)^2 (q_l - k)(q_h - k) = 0. \quad (14)
\end{aligned}$$

Therein, $q_i = \sqrt{k^2 + \frac{n}{\nu_i}}$ and $\alpha_i = \frac{\rho_i}{\rho_l + \rho_h}$. Here, the kinematic viscosity of each fluid is denoted by ν_i , gravity by g and surface tension by T . We follow the setup of Shi et al. [49], hence $T = 0$ and $\mu_l = \rho_l \nu_l = \rho_h \nu_h = \mu_h$. Together with $\alpha_l \nu_l = \frac{\rho_l \nu_l}{\rho_l + \rho_h} = \frac{\rho_h \nu_h}{\rho_l + \rho_h} = \alpha_h \nu_h$ eq. (14) reduces to

$$- \left\{ \frac{gk}{n^2} (\alpha_l - \alpha_h) + 1 \right\} (\alpha_h q_l + \alpha_l q_h - k) - 4k\alpha_l\alpha_h = 0. \quad (15)$$

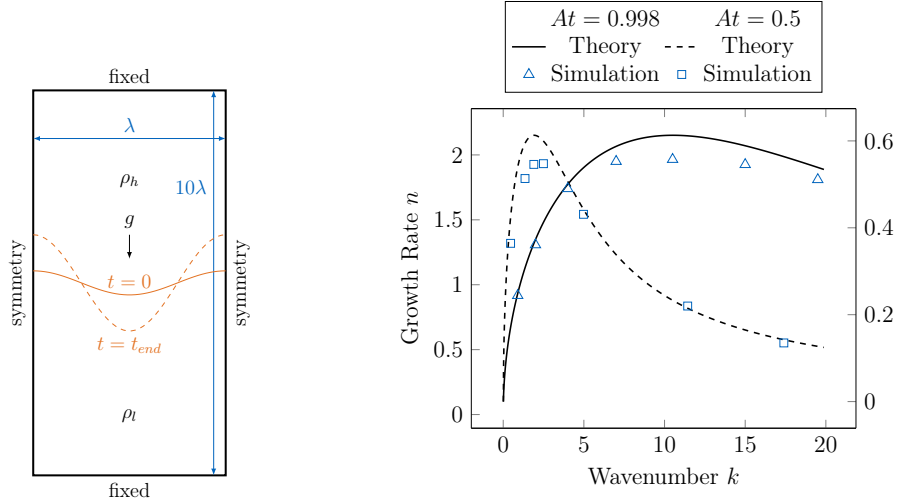
Table 1: Fluid properties for both Atwood numbers used in the RTI growth-rate study.

	$At = 0.5$	$At = 0.998$
ρ_h	1.5	99.9
ρ_l	0.5	0.1
μ	0.1	0.5
g	1.0	1.0
l_{max}	l_3	l_3

We varied the wavenumber $k \in [0, 20]$ for two Atwood numbers $At = \alpha_h - \alpha_l = 0.5$ and $At = 0.998$, which resemble a gas-gas or liquid-gas system, respectively. The detailed setting for each configuration is given in table 1. For all simulations, we adjust the domain size such that the short side spans one respective wavelength $\lambda = 2\pi/k$ while keeping a fixed aspect ratio of 1 to 10 between the short and the long axis. We illustrated the setup in Figure 7a. This yields an effective resolution of 1280 cells for the long side. We disturb the interface initially with a deflection of λ and an amplitude of $0.05/k$. We apply fixed-value boundary conditions at the top and bottom and symmetry conditions otherwise. We monitor the interface displacement $d(t)$ along the vertical centerline, where the position of the maximum density gradient denotes the apparent interface position. The growth rate n thus becomes

$$n = \frac{\partial}{\partial t} \ln \frac{d(t)}{d(0)}. \quad (16)$$

Figure 7b shows a comparison of the growth rates obtained from our simulations and the analytical results from eq. (15) for both Atwood numbers.



(a) Generic case setup used in the growth-rate study. (b) Growth rate over the wavenumber of the initial disturbance. The analytic curve is obtained by solving eq. (15) for each $k = 0, 0.01, \dots, 20.0$.

Figure 7: Case setup for the Rayleigh-Taylor instability (left) and the obtained growth rates in the linear regime (right).

We see that our framework predicts the growth rates very well, which verifies the correctness of the implementation of the viscous source terms and body force contributions.

5.3. Single-core performance

The single-core performance is analyzed for the Sod shock tube problem in a cubic box of size $[0, 1]^3$. We run this test case for ten macro time steps and profile the run with Intel Advisor 2018 Update 4. The test runs take 0.78s wall-clock time. We found that about 91.2% of the runtime is spent in the approximate Riemann solver, which also accounts for 91.4% of the overall floating-point operations (FLOP). The compute-kernel i.e. the main

compute-loop within the Riemann solver runs at 13.71GFLOP s^{-1} and an arithmetic intensity of 0.22FLOP B^{-1} .

The analysis with Advisor revealed that auto-vectorization by the compiler results only in streaming SIMD extensions (SSE) parallelization. Hence, we manually enabled advanced vector extensions (AVX) instructions using the `-xCORE-AVX2` compiler flag. With the higher instruction set, the runtime reduces to 0.68s (-13%) and now the main compute-loop accounts for 79% of the overall runtime. The performance of the main loop increased to 22.82GFLOP s^{-1} , obviously still at 0.22FLOP B^{-1} .

However, it is important to note that the AVX vectorization changes the truncation error of floating-point operations, e. g. by changing the summation order. For our studies of hyperbolic problems with low-dissipation high-resolution schemes, this can strongly affect the simulation results [50]. This effect can be visualized using an inviscid RTI setup with gravity $g = 1$ in y-direction, see [49]. The physical simulation time is $t_{end} = 1.95$ using a CFL number of 0.6 . The effective resolution along the y-axis is set to 8192 cells with $l_{max} = 6$. Figure 8 shows the final time step of this test case with and without the `-xCORE-AVX2` compiler flag. Although we ensured exact symmetry in the initial condition according to [50], we see nonphysical symmetry breaking for the AVX-instructions enabled case.

Aiming for exact reproducibility avoiding numerical artifacts as much as possible, here we sacrifice this performance optimization for the remainder of this work. Note, as shown in [43] the scaling behavior is anyway unaffected by node-level SIMD performance.

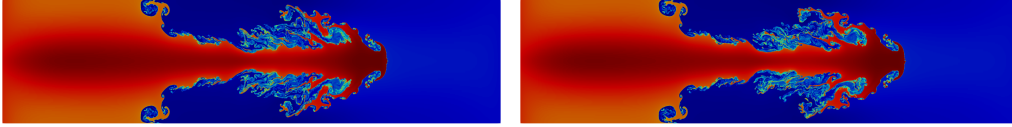


Figure 8: Influence of vectorization on the symmetry of a RTI simulation. In the standard configuration (left) the initial symmetry prevails, whereas for the configuration compiled with AVX instructions (right) it does not.

5.4. *Parallel Performance*

We evaluate the parallel performance for different numerical setups with both strong and weak scaling analyses. Therein, hyper-threading is disabled and we pin one MPI rank to one physical core. Note, we always pin an MPI rank to one physical core, and, hence, use these terms interchangeably. At first we look at the performance implications of choosing the more commonly changed Riemann solvers and reconstruction stencils. Later, we also analyze the effects of more edge-case changes on the parallel performance such as changing the EOS, the SFC or the number of internal cells. We test the latter, configurations in smaller scaling setups using a maximum of eight nodes.

Throughout this section we report averages over three runs for each configuration. Therein, we measure the runtimes using `MPI_Wtime` and neglect time needed for initialization or input/output routines. The standard deviation for all runs was less than 3%. The purpose of this systematic performance analysis for numerical setup permutations is to demonstrate both the flexibility of the presented software framework and the general code efficiency without specific single-purpose tuning.

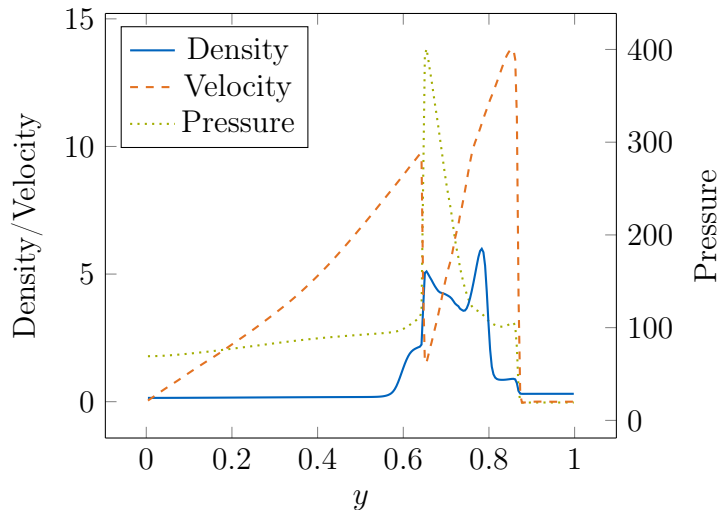


Figure 9: Density, pressure and velocity distribution along the x -axis for the weak scaling case at $t_{end} = 0.38$ using the standard configuration for the resolution described above.

5.5. Weak Scaling

We conduct a weak scaling analysis to measure the influence of changing the Riemann solver or reconstruction stencil on the parallel performance of our implementation. We use the quasi-one-dimensional blast wave case [51] in y -direction as tests case and extend the domain in the other two dimensions linearly with the core count. We set $l_{max} = 3$, with an effective resolution of $128 \times 512 \times 128$ cells in the one-core configuration. The test case is typically ran until $t_{end} = 0.38$. The final states at this point using the standard configuration are depicted in fig. 9.

For our scaling runs we, only compute the first 25 macro time steps. We set $CFL = 0.9$, which allows to cover a maximum of physical time in these 25 steps, and, in turn give a more realistic numerical load as more mesh adaptations are stimulated. Using multiple macro time steps allows

to take changing load due to re-meshing into account which is ubiquitous in real-world physical simulations. We performed the scaling runs using four different setups. The standard configuration, a configuration where only the reconstruction stencil is changed from WENO5 to TENO5, one where only the Riemann solver is changed to LLF, and one where both were changed to HLLC and WENO-WAO53, respectively.

All configurations are run with 1 to 512 cores. The overall runtimes of the single-core configurations were comparable, except for the HLLC one which ran about 30% slower compared to the standard configuration. Note however, that for 512 cores this penalty decreased to only 1% as the overall scaling is best in this configuration. The recorded efficiency is plotted in fig. 10. The scaling behaviors of all configurations are nearly identical with a steep drop in the efficiency when going from 2 to 16 cores. Nevertheless, all configurations show an efficiency plateau from 16 to 256 core, which indicating almost ideal scaling. For all rank numbers HLLC-WAO53 shows the best efficiency. Going above 256 cores we observe a clear drop below an efficiency of 50%.

We see, that modular setup of our solver enabled us to obtain comparable runtimes and weak scaling behaviors across different compute kernels. Nevertheless, configurations with larger compute to communication ratios yield higher efficiencies. So does the more complex reconstruction stencil in the HLLC-WAO53 configuration allows to overlap computation and communication more effectively. Furthermore, we see, a decrease in performance when scaling within one node, i. e. when less than 32 cores are used, but the efficiency remains almost constant when scaling across nodes. We conclude that our MPI-only implementation handles inter-node parallelization more

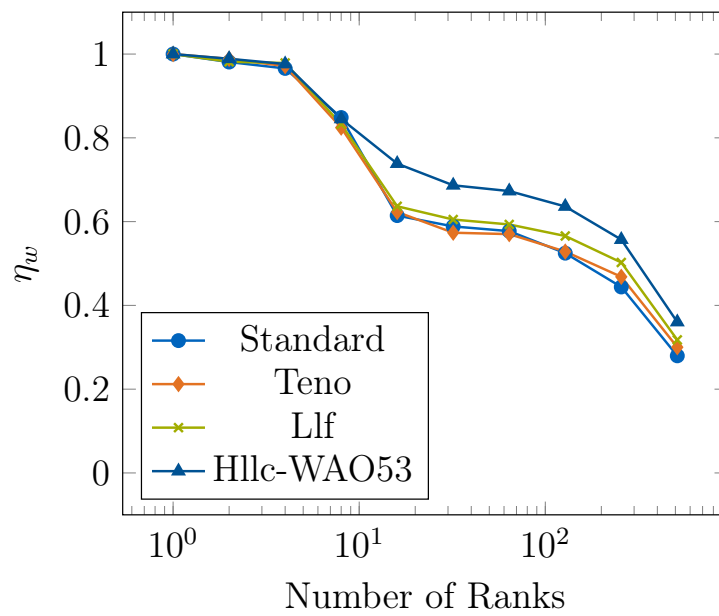


Figure 10: Weak scaling efficiency for different configurations of Riemann solvers, reconstruction stencils and internal cells per block.

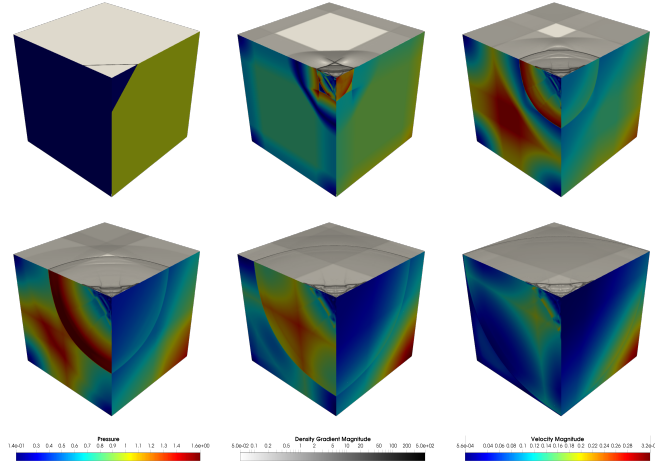


Figure 11: Temporal evolution of the strong-scaling implosion case. From left to right and top to bottom the images show give the time from $t = 0.0$ to $t_{end} = 0.5$ in steps of 0.1. Each depicted cube shows the numerical schlieren, the velocity magnitude and the pressure on the top, left and right face, respectively. The last row gives the used color scales.

efficiently than intra-node parallelization.

5.6. Strong Scaling

Here, we analyse the strong scaling performance for the four numerical configurations used in the weak scaling above. Now, we use a variant of the implosion case of [52] by extending the problem to 3D, giving us a domain of $[0, 0.6]^3$ with symmetry boundary conditions on all sides. The initial discontinuity is placed at $x + y + z = 0.15$. Secondly, we model the fluid to be viscous with $\mu = 1.0e - 6$, and impose a body force acceleration $g = (1, 1, 1)$. The temporal evolution of the pressure, velocity and density field is shown in fig. 11.

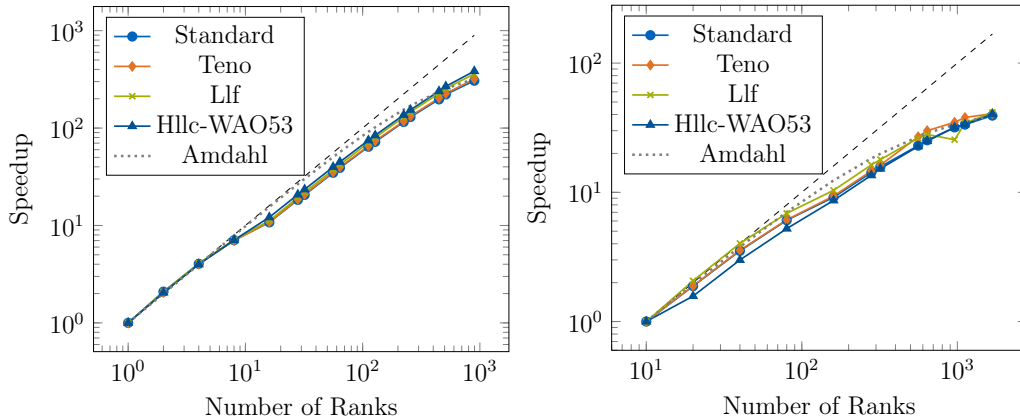


Figure 12: Speedups for the coarse (left) and fine (right) strong scaling cases. The dashed line shows the ideal speedup, and the grey dotted one shows the scaling according to Amdahl's law with a parallel fraction of 99.8%

For the strong scaling runs, we record the compute time needed to advance the simulation from $t = 0.4$ to $t_{end} = 0.5$. We ran the test case in two different resolutions. The lower resolved case holds 512^3 effective cells with $l_{max} = l_4$. The resolution is chosen such that it fits into the memory of a single compute node. The finer-resolved case has a resolution of 1536^3 effective cells with $l_{max} = l_5$. This case requires the memory of at least 10 compute nodes. The finer resolution is needed as the coarser one suffers from under-subscription problems for large core counts. This under-subscription is analyzed in detail in section 5.7. The obtained speedups are shown in fig. 12. For the fine resolution case we take the runtime on ten ranks (spread onto ten nodes) as initial point.

As for the weak scaling, we see that the parallel performance of the different kernels is very similar. The obtained speedups, also drop going from 4 to 16 cores. For higher core counts, i. e. from 32 to 256, a near-ideal speedup

is seen until it finally levels off. The observed speedups indicate a parallel program fraction of $> 99.8\%$ according to Amdahl’s law. Furthermore, we can see that scalability is unaffected whether a node is completely packed or if the MPI ranks are spread out, c.f. points for 28 and 32 or 112 and 128 cores.

5.7. Worst Case Setup

As we have demonstrated the performance of our solver in the last sections, here we look at the performance given an artificial worst case setup. Therefore, we simulate the spherical explosion case of Toro [53, Section 17.1]. It basically resembles a spherical Sod shock tube, c.f. section 5.1. Therein, the initial high pressure and density states are spherically centered in a cubic domain of side length $[0, 2]^3$. As for the Sod shock tube case, we simulate the problem until $t_{end} = 0.2$. We partitioned the domain into three blocks per dimension and set $l_{max} = l_0$. We run this setup using different number of ranks $r = [1; 28]$. In this setup, unfavorable latencies and/or communication patterns are inevitable for certain r . As an example, consider the case of $r = 16$, where eleven ranks hold two blocks, while the remaining five ranks hold only one block. The latter five are, hence, idle half the time. In the case of $r = 27$, each block has a maximum of communication partners; the center block even reaches the theoretical maximum of 27 same-level communication partners. Figure 13 shows the obtained strong scaling efficiency η_s over r . We see a continuous decrease in efficiency until 26 cores are used where the efficiency drops below 50% as soon as more than 16 cores are used. When using 27 cores, however, η_s jumps back to 57%. Confirming our previous assessment. Since we suggest that the performance increase if the blocks are

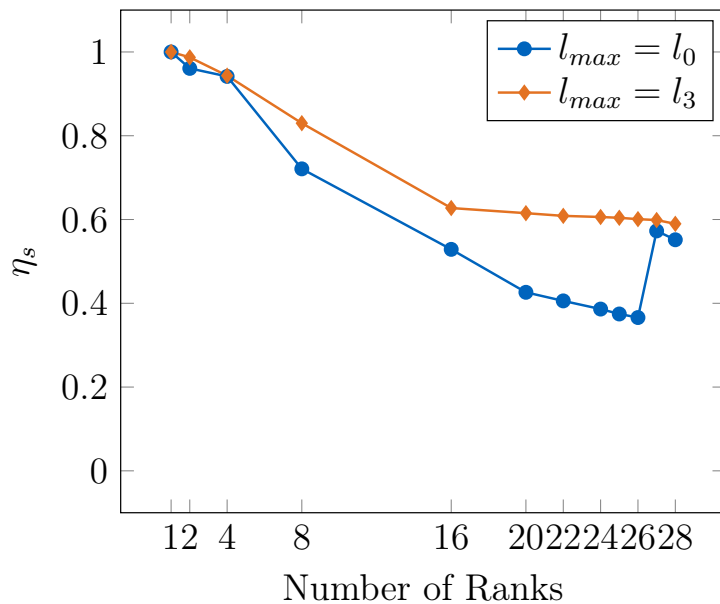


Figure 13: Strong scaling efficiency for a spherical Sod shock tube case. The domain decomposition is artificially set to a worst case scenario for $l_{max} = l_0$. An improved decomposition is obtained by increasing the allowed refinement to $l_{max} = l_3$.

more evenly distributed to the available cores. Therefore, we rerun the case with an increased $l_{max} = l_3$, which creates at least 218 blocks. The obtained efficiency with increased l_{max} is also plotted in fig. 13. We observe that in this case the efficiency is higher for all core counts and remains above 50% at all times, and is in agreement with our earlier assessment.

The conducted test shows the limitations of our block-based MR algorithm for low block to core ratios. When simulation physical problems, however, the block to core ratio is typically one or more orders of magnitude higher [25, 54] than in the cases presented in this section. Hence, these performance limitations are of little significance.

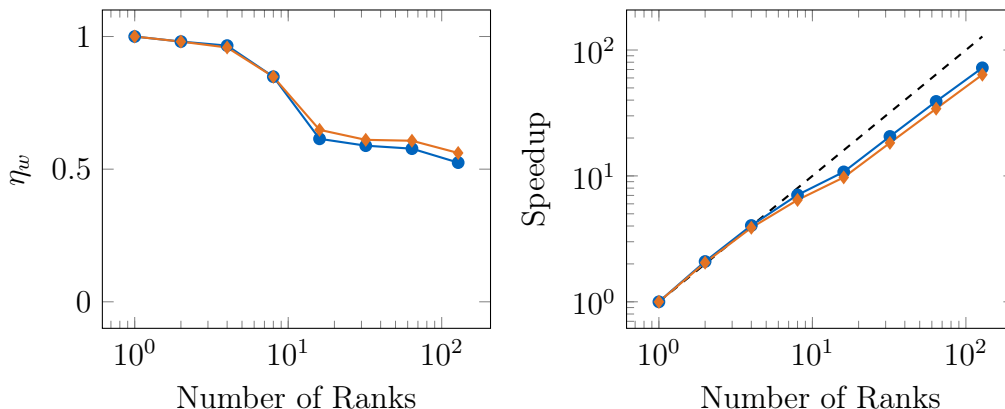


Figure 14: Comparison of weak (left) and strong (right) scaling using two different space-filling curves, namely the Hilbert-curve \bullet and the Z-curve \blacklozenge .

5.8. Influence of Space Filling Curve

In this section, we analyze the performance impact of different SFC, i. e. the level-wise Hilbert curve versus the level-wise Z-Curve. For both configurations, we compare the weak scaling on the test case described in section 5.5 (channel), and the strong scaling on the test case described in section 5.6 (cubic geometry). Following our earlier discussion, here, we limit the core counts from 1 to 128. Figure 14 shows the obtained scaling for the weak (efficiency) and strong (speedup) scaling tests.

We see that the performance of the two types of curves are comparable. However, the Hilbert curve partitioning yields slightly better strong scaling, while the opposite is true for the weak scaling. Despite the scaling behavior being very similar, the Z-curve is always slower in absolute wall-clock runtime. We recorded relative differences from 9.6% to 25% for increasing core counts in the strong-scaling case and, from 11% to 4% in the weak-scaling setup. The obtained results motivate our default selection of the level-wise

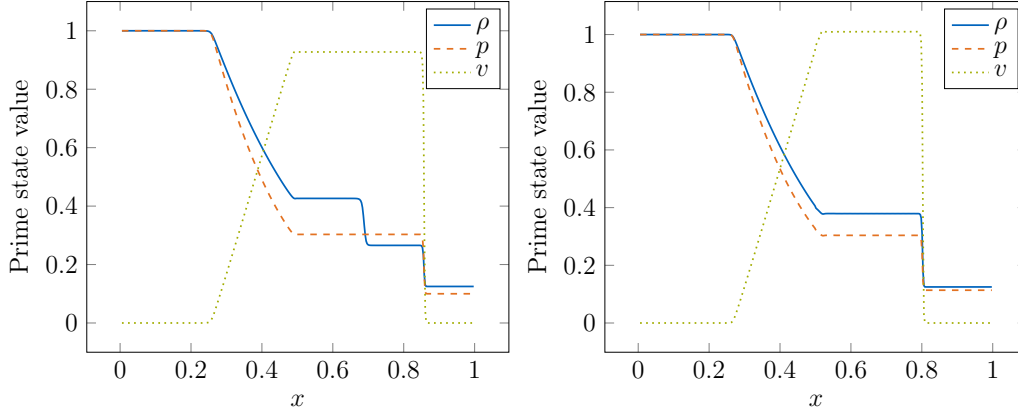


Figure 15: Spatial prime state profile at $t = 0.2$ for the Sod sock tube simulation using different equations of state. The stiffened-gas and Tait's equation are shown on the left and right, respectively.

Hilbert-curve for its runtime advantage over the level-wise Z-curve.

5.9. Influence of Equation of State

Based on the reference results from section 5.1, we test the influence of changing the EOS from stiffened-gas to Tait's [55] on the parallel performance. We restrict the analysis to the case of $l_{max} = 3$. The material parameters are $\gamma = 1.4$, $A = 1.0$, $B = 0.937315$ and $\rho_0 = 1.0$. The prime state profiles at $t_{end} = 0.2$ are shown for both EOS in fig. 15.

With both EOS we conducted a weak-scaling analysis from 1 to 224 cores. The obtained parallel performance is summarized in fig. 16, where we plot the weak-scaling efficiency η_w together with the respective runtimes for different core count. Clearly, the scaling behavior is similar for both EOS, despite a runtime difference of about 18%. As in the large weak scaling study c. f. section 5.5, the efficiency drops to 64% on 16 cores, but remains near ideal for successively higher core counts. As discussed later in section 5.12, also

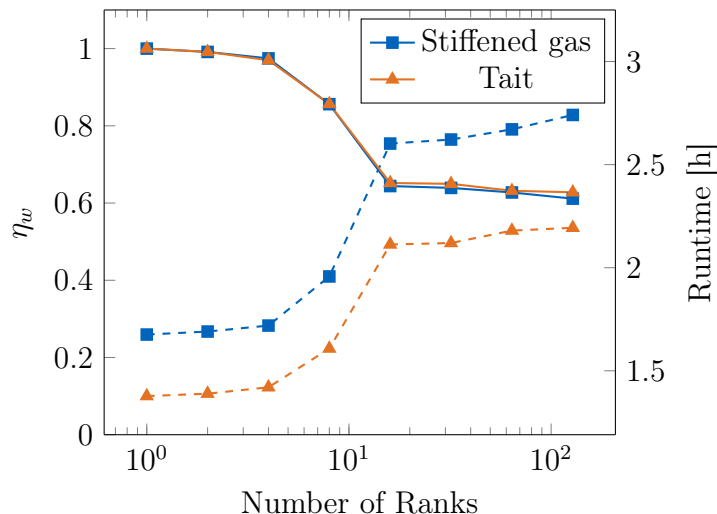


Figure 16: Weak scaling efficiency η_w and absolute runtime for the Sod case using different equations of state. Note, coloring is identical for both graphs. The dashed lines indicates the wall clock time and the solid curves denote η_w .

the compression for both EOS is similar. Overall, the difference in runtime is explained by the reduced amount of computational work as in Tait’s formulation the energy in eq. (1) becomes a dependent variable.

5.10. Influence of Error Norm

We stated earlier that the error norm guiding the MR compression, c. f. eq. (5), can be chosen at compile-time. In this section, we want to analyze the performance impact of different norms. We re-use the RTI case given in section 5.3, but we limit l_{max} to four levels. We chose the inviscid RTI case as it is sensitive to the employed error norm, see fig. 17. Here, we show the density field at $t_{end} = 1.95$ and the resulting mesh.

In order to compare the computational performance of the three setups,

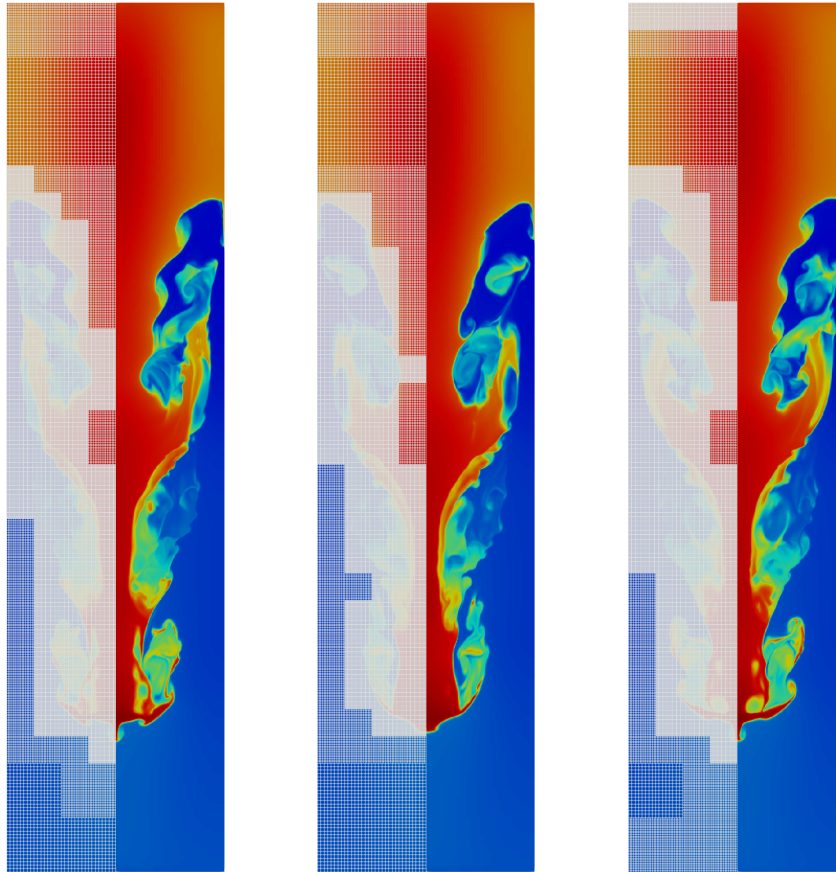


Figure 17: Density field and corresponding mesh at $t = 1.95$ for the inviscid RTI case in the $x - y$ center plane. The color scale ranges from blue $\rho = 0.64$ to red $\rho = 2.4$. From left to right the l_∞ -, l_1 - and l_2 -norms are used, respectively.

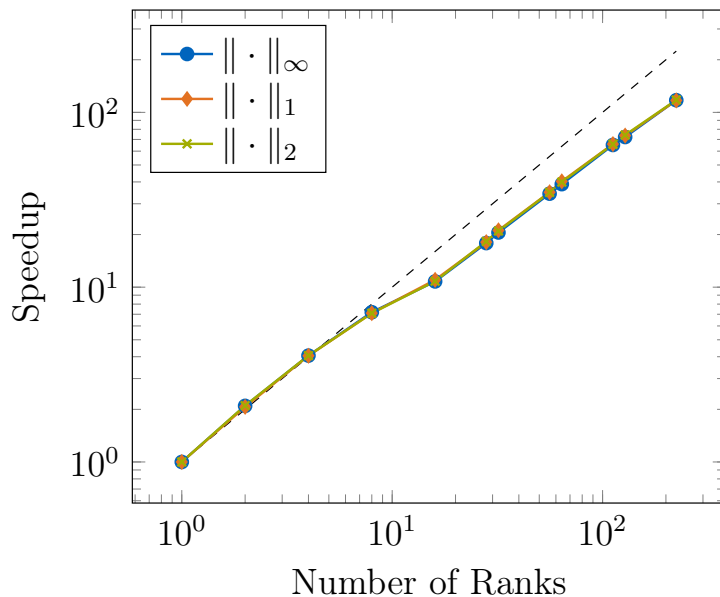


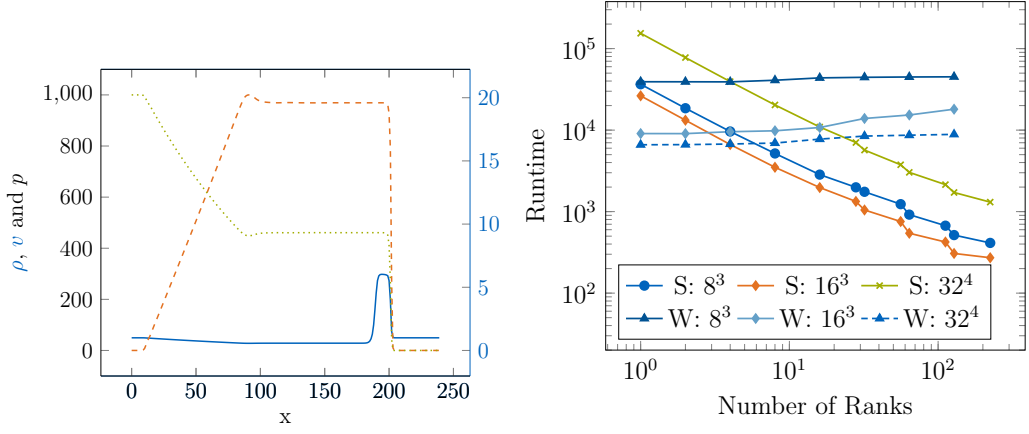
Figure 18: Speedup for the strong scaling analysis of configuration using different refinement norms. The dashed line indicates the ideal speedup.

we tune the respective reference errors ε_{ref} for each case to obtain a comparable number of leaves. For each norm, we conducted a strong scaling analysis from one to eight compute nodes. Therein, we record the wall clock time for the simulation of a developed RTI from $t = 1.90$ until t_{end} . As for the weak-scaling test, we again see in fig. 18 almost ideal speedup using more than 16 cores. For all cases the efficiency stays above 50%, which implies a parallel fraction of the code > 0.99 according to Amdahl's law. Hence, the error norm does not affect the parallel performance itself, despite its strong influence on the resulting mesh topology.

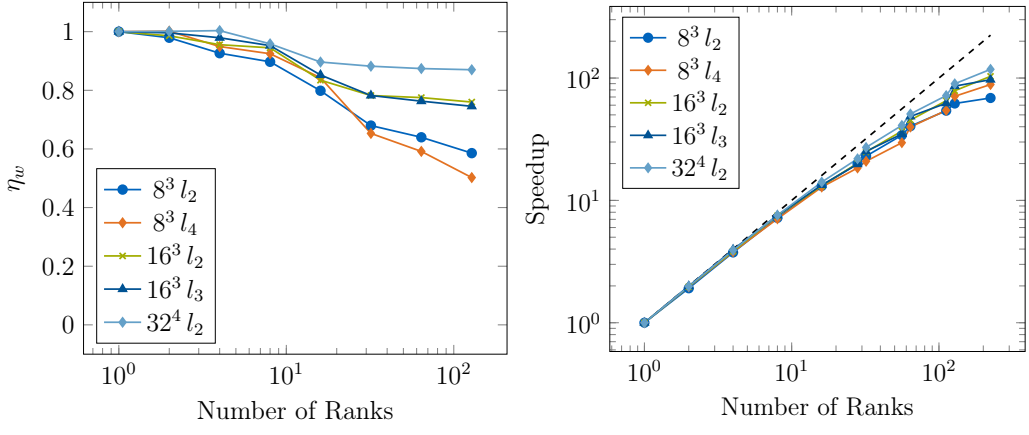
5.11. Influence of Internal Cells per Block

In this section we analyze the effect of the grain size, i. e. the number IC per block. Therefore, we run a weak and strong scaling analysis for “Test 3” of Toro [53, Section 4.3.3]. The final states at $t = 0.012$ are given in fig. 19a. For the strong scaling and the initial configuration of the weak scaling analysis, we use a domain of size $1 \times 0.25 \times 0.25$ and discretized it using four blocks on l_0 with $l_{max} = 2$. For the weak scaling analysis, we increase the superfluous y- and z-dimensions. We use the standard configuration and vary only the IC per block from 8^3 to 16^3 and 32^3 . This results in a four times higher resolved domain for the 32^3 cells per block case compared to the 8^3 one, but the number of nodes and leaves is comparable. In contrast, we also test the configurations with effectively the same resolution. We obtain these same resolutions by increasing l_{max} until the cases with 16^3 and 8^3 IC per block are as fine resolved as the case with 32^3 IC per block. The obtained weak scaling efficiency η_w and strong scaling speedups and the absolute runtimes are given in fig. 19.

We observe that the scaling efficiency/speedup is better the more internal cells per block are used. This is expected as more internal cells improve the ratio of computation-to-communication. However, a closer look at the absolute runtimes shows, that for a case of comparable resolution the configuration using 16^3 IC per block is fastest. On average it outperforms the one using 8^3 IC per block by over 50%. We attribute this speedup to the improved computation-to-communication ratio. In comparison to 32^3 IC per block the performance improves even by 450%. The reason for this tremendous difference can be found in the compression, see the following section 5.12.



(a) Density —, pressure and velocity - - - along the x -axis for "Test 3" of Toro at $t = 0.012$. (b) Runtimes for the case with same effective resolutions using different number of internal cells per block. The type of scaling weak (W) and strong (S) is abbreviated in the legend.



(c) Weak scaling efficiency for different number of internal cells per block. The used maximum level is denoted in the legend. (d) Strong scaling speedups for different number of internal cells per block. The used maximum level is denoted in the legend.

Figure 19: Final states, scaling efficiency, speedup and runtimes when using different number of internal cells per block.

5.12. Compression

Finally we analyze at the compression of our block-based MR algorithm for the presented cases. We define the memory-compression C as the ratio between the number of cells actually present in the simulation, and the *effective* number of cells via

$$C = 1 - \frac{\#\text{cells}}{\#\text{effective cells}}. \quad (17)$$

Note that the compression of flux function computations is proportional to the memory compression.

According to this definition we strive for high values of C . We plot the achieved compression of the cases used above as function over the relative simulation time in Figure 20. Besides the test case name also the respective l_{max} is given. The case names are abbreviated as follows: ‘Weak’, ‘Strong’, ‘RTI’ and ‘Sod’ correspond to the cases of sections 5.1, 5.3, 5.5 and 5.6. ‘Stiff’ and ‘Tait’ refer to the used EOS in section 5.9 and x^3 with $x \in 8, 16, 32$ stands for the number of IC per block as defined and used in section 5.11. If we look at the Sod cases, we see how the compression increases with l_{max} . For $l_{max} = l_0$, obviously, no compression is achieved. With $l_{max} = l_3$, the average compression is already at 50%. Nevertheless, in the final time steps most of the domain gets refined, reducing compression significantly. With a further increase of l_{max} , the compression increases drastically. In the ‘RTI’ case the compression reduces monotonically as the initial disturbance grows and generates more and more finer scales. Nevertheless, an average compression of 75% is achieved. For the different EOS, the achieved compression is very similar. Hence, differences in the runtimes as stated above may not be

credited to unequal compression. In the case of varying IC per block, the effect of increasing the level of refinement is again clearly visible: While the cases using $l_{max} = l_3$ and l_4 achieved similar compressions above 80%, the case with $l_{max} = l_2$ gives much smaller compression. Furthermore, the lack of levels prohibits effective adaptation to changes in the flow field and the compression remains almost constant over the whole simulation time. In contrast to the other cases, here the compression fluctuates, showing that the mesh quickly adapts to changes in the flow. In the ‘weak’ case we also observe similar characteristics as for the Sod cases with the same maximum level of refinement. The compression rate is high on average, but in the case where multiple distinct waves travel through the domain the compression drops. For the weak case this is visible at the beginning of the simulation. Once the waves collide in the middle of the domain, the compression increases again. The ‘strong’ case shows a combination of the effects observed in the other cases. In the beginning, compression is reduced by the outward travelling of different shock waves, then additionally, smaller scales are formed at the initial discontinuity. Towards the end, the compression reaches a deflection point as no more strong shocks are generated and the viscous effects start to smooth the flow field.

Overall, detailed analysis demonstrates that our block-based implementation achieves high compression rates if l_{max} is chosen sufficiently large. In particular for 3D simulations, the compression of our block-based scheme is comparable to those reported for cell-based MR algorithms [14, 15, 18, 19, 26].

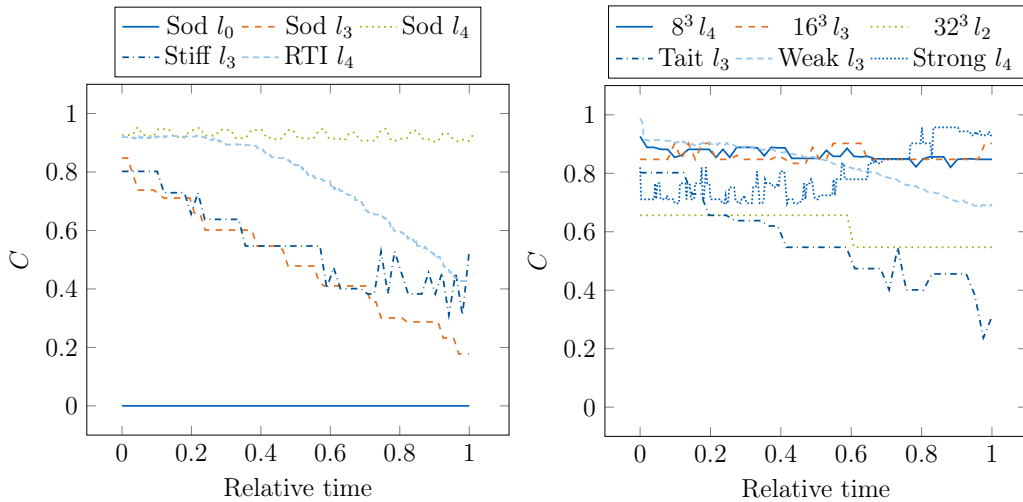


Figure 20: Compression of different test cases over time. The compression values are sampled after each completed macro time step. For better readability, the cases are split into two figures. The used l_{max} for each case is indicated.

6. Conclusion

We have presented a MPI parallelization strategy for a 3D block-based MR algorithm with ALTS for the simulation of the compressible Euler or Navier-Stokes equations. Our scheme allows to bisect the underlying octree structure arbitrarily. This is achieved by introducing a modified Morton order and level-wise SFC-based load balancing. The achieved compression in 3D of our block-based approach is comparable to cell-based approaches. The presented strategy was implemented in a modular C++ framework, a detailed description of the implementation is given. The modular framework was validated with multiple test cases and its (parallel) performance was assessed thoroughly for varying compute kernels by means of weak and strong scaling analyses up to 1680 cores. Our implementation shows reasonable parallel

performance and is able to deliver similar performance for a range of differing kernels. The presented framework is available under open-source licence.

In future work the performance of the scheme is to be improved further. This could be achieved by further optimizing the load balancing strategy and exploiting further SIMD-capabilities, or by reducing the MPI overhead via an additional shared-memory hybrid parallelization, e. g., with Open Multi-Processing (openMP).

7. Acknowledgment

The authors would like to thank Felix Späth for his help in the implementation of the SFC and the communication cache. The first author would like to further thank Vladimir Bogdanov for helping with the bit-wise logic operations.

The authors have received funding from the European Research Council (ERC) under the European Union’s Horizon 2020 research and innovation programme (grant agreement No. 667483).

The authors gratefully acknowledge the Gauss Centre for Supercomputing e.V. for funding this project by providing computing time on the CoolMUC-2 Linux-Cluster at Leibniz Supercomputing Centre.

The authors acknowledge the Bavarian State Ministry of Science and the Arts for partial funding through the Competence Network for Scientific High Performance Computing in Bavaria (KONWIHR).

Appendix A. Definitions of Q -terms

In the prediction equation eq. (9) we skipped the Q -terms for brevity. Here, their definition is given in full for a 5th-order accurate Prediction as used throughout this paper. In the definitions u_{ijk} refers to the parent that is the base of the prediction and we drop the level-indicating subscript for better readability.

$$c_0 = -\frac{22}{128}, \quad c_1 = \frac{3}{128},$$

$$c_{pq} = c_p c_q \forall (p, q) \in [0, 1]$$

$$c_{rpq} = c_r c_p c_q \forall (r, p, q) \in [0, 1]$$

$$Q_x = c_0 (u_{i+1,j,k} - u_{i-1,j,k}) + c_1 (u_{i+2,j,k} - u_{i-2,j,k})$$

$$Q_y = c_0 (u_{i,j+1,k} - u_{i,j-1,k}) + c_1 (u_{i,j+2,k} - u_{i,j-2,k})$$

$$Q_z = c_0 (u_{i,j,k+1} - u_{i,j,k-1}) + c_1 (u_{i+2,j,k+2} - u_{i,j,k-2})$$

$$\begin{aligned}
Q_{xy} = & c_{00} [(u_{i+1,j+1,k} + u_{i-1,j-1,k}) - (u_{i-1,j+1,k} + u_{i+1,j-1,k})] \\
& + c_{11} [(u_{i+2,j+2,k} + u_{i-2,j-2,k}) - (u_{i-2,j+2,k} + u_{i+2,j-2,k})] \\
& + c_{01} [(u_{i+1,j+2,k} + u_{i-1,j-2,k}) - (u_{i-1,j+2,k} + u_{i+1,j-2,k})] \\
& + c_{10} [(u_{i+2,j+1,k} + u_{i-2,j-1,k}) - (u_{i-2,j+1,k} + u_{i+2,j-1,k})]
\end{aligned}$$

$$\begin{aligned}
Q_{xz} = & c_{00} [(u_{i+1,j,k+1} + u_{i-1,j,k-1}) - (u_{i-1,j,k+1} + u_{i+1,j,k-1})] \\
& + c_{11} [(u_{i+2,j,k+2} + u_{i-2,j,k-2}) - (u_{i-2,j,k+2} + u_{i+2,j,k-2})] \\
& + c_{01} [(u_{i+1,j,k+2} + u_{i-1,j,k-2}) - (u_{i-1,j,k+2} + u_{i+1,j,k-2})] \\
& + c_{10} [(u_{i+2,j,k+1} + u_{i-2,j,k-1}) - (u_{i-2,j,k+1} + u_{i+2,j,k-1})]
\end{aligned}$$

$$\begin{aligned}
Q_{yz} = & c_{00} [(u_{i,j+1,k+1} + u_{i,j-1,k-1}) - (u_{i,j-1,k+1} + u_{i,j+1,k-1})] \\
& + c_{11} [(u_{i,j+2,k+2} + u_{i,j-2,k-2}) - (u_{i,j-2,k+2} + u_{i,j+2,k-2})] \\
& + c_{01} [(u_{i,j+1,k+2} + u_{i,j-1,k-2}) - (u_{i,j-1,k+2} + u_{i,j+1,k-2})] \\
& + c_{10} [(u_{i,j+2,k+1} + u_{i,j-2,k-1}) - (u_{i,j-2,k+1} + u_{i,j+2,k-1})]
\end{aligned}$$

$$\begin{aligned}
Q_{xyz} = & c_{000} \left[(u_{i+1,j+1,k+1} - u_{i-1,j-1,k-1}) + (u_{i+1,j-1,k-1} - u_{i-1,j+1,k+1}) \right. \\
& \left. + (u_{i-1,j-1,k+1} - u_{i+1,j+1,k-1}) + (u_{i-1,j+1,k-1} - u_{i+1,j-1,k+1}) \right] \\
& + c_{111} \left[(u_{i+2,j+2,k+2} - u_{i-2,j-2,k-2}) + (u_{i-2,j-2,k+2} - u_{i+2,j+2,k-2}) \right. \\
& \left. + (u_{i+2,j-2,k-2} - u_{i-2,j+2,k+2}) + (u_{i-2,j+2,k-2} - u_{i+2,j-2,k-2}) \right] \\
& + c_{001} \left[(u_{i+1,j+1,k+2} - u_{i-1,j-1,k-2}) + (u_{i-1,j-1,k+2} - u_{i+1,j+1,k-2}) \right. \\
& \left. + (u_{i+1,j-1,k-2} - u_{i-1,j+1,k+2}) + (u_{i-1,j+1,k-2} - u_{i+1,j-1,k+2}) \right] \\
& + c_{110} \left[(u_{i+2,j+2,k+1} - u_{i-2,j-2,k-1}) + (u_{i-2,j-2,k+1} - u_{i+2,j+2,k-1}) \right. \\
& \left. + (u_{i+2,j-2,k-1} - u_{i-2,j+2,k+1}) + (u_{i-2,j+2,k-1} - u_{i+2,j-2,k+1}) \right] \\
& + c_{011} \left[(u_{i+1,j+2,k+2} - u_{i-1,j-2,k-2}) + (u_{i-1,j-2,k+2} - u_{i+1,j+2,k-2}) \right. \\
& \left. + (u_{i+1,j-2,k-2} - u_{i-1,j+2,k+2}) + (u_{i-1,j+2,k-2} - u_{i+1,j-2,k+2}) \right] \\
& + c_{100} \left[(u_{i+2,j+1,k+1} - u_{i-2,j-1,k-1}) + (u_{i-2,j-1,k+1} - u_{i+2,j+1,k-1}) \right. \\
& \left. + (u_{i+2,j-1,k-1} - u_{i-2,j+1,k+1}) + (u_{i-2,j+1,k-1} - u_{i+2,j-1,k+1}) \right] \\
& + c_{010} \left[(u_{i+1,j+2,k+1} - u_{i-1,j-2,k-1}) + (u_{i-1,j-2,k+1} - u_{i+1,j+2,k-1}) \right. \\
& \left. + (u_{i+1,j-2,k-1} - u_{i-1,j+2,k+1}) + (u_{i-1,j+2,k-1} - u_{i+1,j-2,k+1}) \right] \\
& + c_{101} \left[(u_{i+2,j+1,k+2} - u_{i-2,j-1,k-2}) + (u_{i-2,j-1,k+2} - u_{i+2,j+1,k-2}) \right. \\
& \left. + (u_{i+2,j-1,k-2} - u_{i-2,j+1,k+2}) + (u_{i-2,j+1,k-2} - u_{i+2,j-1,k+2}) \right]
\end{aligned}$$

References

- [1] G.-S. Jiang, Shu, Efficient implementation of weighted ENO schemes, *Journal of Computational Physics* 126 (1996) 202–228.
- [2] J. B. Bell, P. Colella, J. A. Trangenstein, Higher order godunov methods for general systems of hyperbolic conservation laws, *Journal of Computational Physics* 82 (2) (1989) 362–397.

- [3] R. B. Pember, J. B. Bell, P. Colella, W. Y. Curtchfield, M. L. Welcome, An adaptive cartesian grid method for unsteady compressible flow in irregular regions, *Journal of Computational Physics* 120 (2) (1995) 278–304, cited By :242.
- [4] V. A. Titarev, E. F. Toro, Finite-volume WENO schemes for three-dimensional conservation laws, *Journal of Computational Physics* 201 (1) (2004) 238–260. doi:10.1016/j.jcp.2004.05.015.
- [5] E. Johnsen, T. Colonius, Implementation of WENO schemes in compressible multicomponent flow problems, *J. Comput. Phys.* 219 (2) (2006) 715–732. doi:10.1016/j.jcp.2006.04.018.
- [6] M. J. Berger, P. Colella, Local Adaptive Mesh Refinement for Shock Hydrodynamics, *J. Comput. Phys.* 82 (1989) 64–84.
- [7] R. Deiterding, M. O. Domingues, K. Schneider, Multiresolution analysis as a criterion for effective dynamic mesh adaptation—a case study for euler equations in the samr framework amroc, *Computers & Fluids* (2020) 104583.
- [8] K. Schneider, O. V. Vasilyev, Wavelet Methods in Computational Fluid Dynamics, *Annual Review of Fluid Mechanics* 42 (1) (2010) 473–503. doi:10.1146/annurev-fluid-121108-145637.
- [9] O. V. Vasilyev, C. Bowman, Second-Generation Wavelet Collocation Method for the Solution of Partial Differential Equations, *Journal of Computational Physics* 165 (2) (2000) 660–693. doi:10.1006/JCPH.2000.6638.

- [10] J. D. Regele, O. V. Vasilyev, An adaptive wavelet-collocation method for shock computations, *International Journal of Computational Fluid Dynamics* 23 (7) (2009) 503–518. doi:10.1080/10618560903117105.
- [11] O. V. Vasilyev, Solving multi-dimensional evolution problems with localized structures using second generation wavelets, *International Journal of Computational Fluid Dynamics* 17 (2) (2003) 151–168. doi:10.1080/1061856021000011152.
- [12] J. M. Alam, N. K.-R. Kevlahan, O. V. Vasilyev, Simultaneous space–time adaptive wavelet solution of nonlinear parabolic differential equations, *Journal of Computational Physics* 214 (2) (2006) 829–857. doi:10.1016/J.JCP.2005.10.009.
- [13] A. Nejadmalayeri, A. Veizolainen, E. Brown-Dymkoski, O. V. Vasilyev, Parallel adaptive wavelet collocation method for PDEs, *Journal of Computational Physics* 298 (2015) 237–253. doi:10.1016/j.jcp.2015.05.028.
- [14] A. Harten, Multiresolution algorithms for the numerical solution of hyperbolic conservation laws, *Communications on Pure and Applied Mathematics* 48 (12) (1995) 1305–1342. doi:10.1002/cpa.3160481201.
- [15] B. L. Bihari, Multiresolution schemes for conservation laws with viscosity, *Journal of Computational Physics* 123 (1) (1996) 207–225. doi:10.1006/jcph.1996.0017.
- [16] B. L. Bihari, A. Harten, Multiresolution schemes for the numerical solution of 2-D conservation laws I, *SIAM Journal on Scientific Computing* 18 (2) (1997) 315–354.

- [17] M. K. Kaibara, S. M. Gomes, A Fully Adaptive Multiresolution Scheme for Shock Computations, in: *Godunov Methods*, Springer US, Boston, MA, 2001, pp. 497–503. doi:10.1007/978-1-4615-0663-8_49.
- [18] A. Cohen, S. Kaber, S. Müller, M. Postel, Fully adaptive multiresolution finite volume schemes for conservation laws, *Mathematics of Computation* 72 (241) (2003) 183–225.
- [19] O. Roussel, K. Schneider, A. Tsigulin, H. Bockhorn, A conservative fully adaptive multiresolution algorithm for parabolic PDEs, *Journal of Computational Physics* 188 (2) (2003) 493–523. doi:10.1016/S0021-9991(03)00189-X.
- [20] D. A. Castro, S. M. Gomes, J. Stolfi, High-order adaptive finite-volume schemes in the context of multiresolution analysis for dyadic grids, *Computational and Applied Mathematics* 35 (1) (2016) 1–16. doi:10.1007/s40314-014-0159-2.
- [21] R. Maulik, O. San, R. Behera, An adaptive multilevel wavelet framework for scale-selective WENO reconstruction schemes, *International Journal for Numerical Methods in Fluids* (January) (2018) 1–31. doi:10.1002/flid.4489.
- [22] S. Müller, Y. Stiriba, Fully Adaptive Multiscale Schemes for Conservation Laws Employing Locally Varying Time Stepping, *Journal of Scientific Computing* 30 (3) (2007) 493–531. doi:10.1007/s10915-006-9102-z.
- [23] M. O. Domingues, S. M. Gomes, O. Roussel, K. Schneider, An adaptive multiresolution scheme with local time stepping for evolutionary

- PDEs, *Journal of Computational Physics* 227 (8) (2008) 3758–3780. doi:10.1016/j.jcp.2007.11.046.
- [24] M. O. Domingues, S. M. Gomes, O. Roussel, K. Schneider, Space–time adaptive multiresolution methods for hyperbolic conservation laws: Applications to compressible Euler equations, *Applied Numerical Mathematics* 59 (9) (2009) 2303–2321. doi:10.1016/j.apnum.2008.12.018.
- [25] J. W. J. Kaiser, N. Hoppe, S. Adami, N. A. Adams, An adaptive local time-stepping scheme for multiresolution simulations of hyperbolic conservation laws, *Journal of Computational Physics: X* 4 (2019) 100038.
- [26] S. Descombes, M. Duarte, T. Dumont, T. Guillet, V. Louvet, M. Massot, Task-based adaptive multiresolution for time-space multi-scale reaction-diffusion systems on multi-core architectures, *The SMAI journal of computational mathematics* 3 (2017) 29–51. doi:10.5802/smai-jcm.19.
- [27] K. Brix, S. Melian, S. Müller, M. Bachmann, Adaptive Multiresolution Methods: Practical issues on Data Structures, Implementation and Parallelization, *ESAIM: Proceedings* 34 (2011) 151–183. doi:10.1051/proc/201134003.
- [28] H. Sutter, The free lunch is over: A fundamental turn toward concurrency in software, *Dr. Dobb’s Journal* (2005) 1–9doi:10.1002/minf.201100042.
- [29] G. Hager, G. Wellein, Introduction to high performance computing for scientists and engineers, CRC Press, 2011.

- [30] C. R. Ferreira, M. Bader, Load Balancing and Patch-Based Parallel Adaptive Mesh Refinement for Tsunami Simulation on Heterogeneous Platforms Using Xeon Phi Coprocessors, in: Proceedings of the Platform for Advanced Scientific Computing Conference on - PASC '17, ACM Press, New York, New York, USA, 2017, pp. 1–12. doi:10.1145/3093172.3093237.
- [31] B. Hejazialhosseini, D. Rossinelli, M. Bergdorf, P. Koumoutsakos, High order finite volume methods on wavelet-adapted grids with local time-stepping on multicore architectures for the simulation of shock-bubble interactions, *Journal of Computational Physics* 229 (22) (2010) 8364–8383. doi:10.1016/j.jcp.2010.07.021.
- [32] L. H. Han, T. Indinger, X. Y. Hu, N. A. Adams, Wavelet-based adaptive multi-resolution solver on heterogeneous parallel architecture for computational fluid dynamics, in: *Computer Science - Research and Development*, Vol. 26, 2011, pp. 197–203. doi:10.1007/s00450-011-0167-z.
- [33] M. Sroka, T. Engels, P. Krah, S. Mutzel, K. Schneider, J. Reiss, An Open and Parallel Multiresolution Framework Using Block-Based Adaptive Grids, Springer, Cham, 2019, pp. 305–319. doi:10.1007/978-3-319-98177-2_19.
- [34] P. L. Roe, Approximate Riemann solvers, parameter vectors, and difference schemes, *Journal of computational physics* 43 (2) (1981) 357–372.
- [35] V. V. Rusanov, The calculation of the interaction of non-stationary

- shock waves and obstacles, *USSR Computational Mathematics and Mathematical Physics* 1 (2) (1962) 304–320.
- [36] E. F. Toro, M. Spruce, W. Speares, Restoration of the contact surface in the HLL-Riemann solver, *Shock waves* 4 (1) (1994) 25–34.
- [37] L. Fu, X. Y. Hu, N. A. Adams, A family of high-order targeted ENO schemes for compressible-fluid simulations, *Journal of Computational Physics* 305 (2016) 333–359. doi:10.1016/j.jcp.2015.10.037.
- [38] D. S. Balsara, S. Garain, C.-W. Shu, An efficient class of WENO schemes with adaptive order, *Journal of Computational Physics* 326 (2016) 780–804. doi:10.1016/j.jcp.2016.09.009.
- [39] G. Morton, A computer oriented geodetic data base and a new technique in the file sequencing (1966) 20.
- [40] F. Harlow, A. Amsden, Fluid dynamics, Tech. rep., Los Alamos National Labs (1971).
- [41] Weighted Essentially Non-oscillatory Schemes, *Journal of Computational Physics* 115 (1994) 200–212. doi:10.1006/jcph.1994.1187.
- [42] D. Rossinelli, B. Hejazialhosseini, D. G. Spampinato, P. Koumoutsakos, Multicore/multi-gpu accelerated simulations of multiphase compressible flows using wavelet adapted grids, *SIAM Journal on Scientific Computing* 33 (2) (2011) 512–540.
- [43] N. Hoppe, I. Pasichnyk, M. Allalen, S. Adami, N. A. Adams, Node-level optimization of a 3D block-based multiresolution compressible flow

- solver with emphasis on performance portability, in: 2019 International Conference on High Performance Computing Simulation (HPCS), 2019, pp. 732–740. doi:10.1109/HPCS48598.2019.9188088.
- [44] M. Bader, Space-Filling Curves, Vol. 9 of Texts in Computational Science and Engineering, Springer Berlin Heidelberg, Berlin, Heidelberg, 2013. doi:10.1007/978-3-642-31046-1.
- [45] D. Hilbert, Über die stetige Abbildung einer Linie auf ein Flächenstück, *Math. Ann.* 38 (1891) 459–460.
- [46] G. A. Sod, A survey of several finite difference methods for systems of nonlinear hyperbolic conservation laws, *Journal of Computational Physics* 27 (1) (1978) 1–31. doi:10.1016/0021-9991(78)90023-2.
- [47] W. J. Harrison, The influence of viscosity on the oscillations of superposed fluids, *Proceedings of the London Mathematical Society* s2-6 (1) (1908) 396–405. doi:10.1112/plms/s2-6.1.396.
- [48] S. Chandrasekhar, Hydrodynamic and hydromagnetic stability, 1961.
- [49] J. Shi, Y. T. Zhang, C. W. Shu, Resolution of high order WENO schemes for complicated flow structures, *Journal of Computational Physics* 186 (2) (2003) 690–696. doi:10.1016/S0021-9991(03)00094-9.
- [50] N. Fleischmann, S. Adami, N. A. Adams, Numerical Symmetry-Preserving Techniques for Low-Dissipation Shock-Capturing Schemes, *Computers & Fluids* (may 2019). doi:10.1016/j.compfluid.2019.04.004.

- [51] P. Woodward, P. Colella, The numerical simulation of two-dimensional fluid flow with strong shocks (apr 1984). doi:10.1016/0021-9991(84)90142-6.
- [52] R. Liska, B. Wendroff, Comparison of Several Difference Schemes on 1D and 2D Test Problems for the Euler Equations, *SIAM Journal on Scientific Computing* 25 (3) (2003) 995–1017. arXiv:0911.1613, doi:10.1137/S1064827502402120.
- [53] E. F. Toro, Riemann solvers and numerical methods for fluid dynamics: a practical introduction, 3rd Edition, Springer, Dordrecht ; New York, 2009.
- [54] J. Winter, J. Kaiser, S. Adami, N. Adams, Numerical investigation of 3d drop-breakup mechanisms using a sharp interface level-set method, in: 11th International Symposium on Turbulence and Shear Flow Phenomena, TSFP 2019, 2019.
- [55] R. P. Fedkiw, T. D. Aslam, B. Merriman, S. Osher, A Non-oscillatory Eulerian Approach to Interfaces in Multimaterial Flows (The Ghost Fluid Method), *Journal of Computational Physics* 152 (1999) 457–492.